Iron versus Ruthenium: Dramatic Changes in Electronic Structure Result from Replacement of One Fe by Ru in [{Cp*(dppe)Fe}-CC-CC-{Fe(dppe)Cp*}]$^{n+}$ (n = 0, 1, 2)

Michael I. Bruce,*[,†] Karine Costuas,[‡] Thomas Davin,[‡] Benjamin G. Ellis,[†,§] Jean-François Halet,*[,‡] Claude Lapinte,*[,§] Paul J. Low,[⊥] Mark E. Smith,[†,§] Brian W. Skelton,[∥] Loic Toupet,[#] and Allan H. White[∥]

Department of Chemistry, University of Adelaide, Adelaide, South Australia 5005, Australia, Laboratoire de Chimie du Solide et Inorganique Moléculaire, UMR 6511, CNRS-Université de Rennes 1, Institut de Chimie de Rennes, 35042 Rennes Cedex, France, Organometalliques et Catalyse: Chimie et Electrochimie Moléculaire, UMR 6509, CNRS-Université de Rennes 1, Institut de Chimie de Rennes, 35042 Rennes Cedex, France, Department of Chemistry, University of Durham, South Road, Durham DH1 3LE, England, Chemistry M313, University of Western Australia, Crawley, Western Australia 6009, Australia, and Groupe Matière Condensée et Matériaux, UMR CNRS 6626, Campus de Beaulieu, Université de Rennes 1, 35042 Rennes Cedex, France

Received April 18, 2005

The reactions of FeCl(dppe)Cp* and Ru(C≡CC≡CH)L_2Cp′ with Na[BPh_4] and 1,8-diazabicyclo[5.4.0]undec-7-ene (dbu; 2 equiv) in a mixed thf/NEt_3 solvent afford {Cp*(dppe)-Fe}(C≡CC≡C){Ru(PP)Cp′} (PP = dppe, Cp′ = Cp*, **7**; PP = $(PPh_3)_2$, Cp′ = Cp, **8**). Cyclic voltammetry shows that these mixed Fe/Ru complexes undergo sequential loss of up to three electrons, with the mono- and dioxidized species being isolated following chemical oxidation. Computational (DFT) and spectroscopic (IR, NMR, ESR, Mössbauer) studies are consistent with a polarized ground-state structure with oxidation leading to the gradual evolution of cumulenic character in the FeC_4Ru moiety and a greater degree of orbital mixing between the Fe, C, and Ru centers than found in the related heterometallic complex [{Cp*(dppe)-Fe}(C≡CC≡C){Re(NO)(PPh_3)Cp*}]$^{n+}$ ([**6**]$^{n+}$). In contrast to the two-electron oxidation products derived from the diiron complex {Cp*(dppe)Fe}(C≡CC≡C){Fe(dppe)Cp*} (**1**) and iron/rhenium complex **6**, the dications [**7**]$^{2+}$ and [**8**]$^{2+}$ feature a dominant contribution from a singlet ground state. Thus, while **6** behaves in a manner closely related to **1**, **7** and **8** are more closely related to {Cp($Ph_3P)_2$Ru}(C≡CC≡C){Ru($PPh_3)_2$Cp} (**2**) and {Cp*(dppe)Ru}-(C≡CC≡C){Ru(dppe)Cp*} (**3**), clearly demonstrating the pronounced role that choice of metal as well as formal electron count can play in tuning the electronic and magnetic properties of this fascinating class of compound.

Introduction

There is much contemporary interest in molecules containing unsaturated carbon chains end-capped by transition metal−ligand groups.[1,2] A considerable body of work is centered on complexes containing end-groups such as $MnI(dmpe)_2$,[3] Re(NO)(PPh_3)Cp*,[4] $Fe(CO)_2$Cp*,[5] Fe(PP)Cp* (PP = dppe, dippe),[6,7] and Ru(PP)Cp′ [PP = (PPh_3)(PR_3), R = Me, Ph; dppm, dppe; Cp′ = Cp, Cp*][8] in complexes of the type {L_xM}(C≡C)$_n${ML_x} (n = 1−10), all of which have been demonstrated to undergo several stepwise one-electron oxidations. Their electronic structures have attracted attention, with theoretical calcula-

* To whom correspondence should be addressed. (J.-F.H.) E-mail: halet@univ-rennes1.fr. Fax: + 33 2 23 23 68 40. (M.I.B.) E-mail: michael.bruce@adelaide.edu.au. Fax: + 61 8 8303 4358. (C.L.) E-mail: lapinte@univ.rennes1.fr. Fax: + 33 2 23 23 59 67.

† University of Adelaide.

‡ Laboratoire de Chimie du Solide et Inorganique Moléculaire.

§ Organometalliques et Catalyse: Chimie et Electrochimie Moléculaire.

⊥ University of Durham.

∥ University of Western Australia.

Groupe Matière Condensée et Matériaux.

(1) Bruce, M. I.; Low, P. J. *Adv. Organomet. Chem.* **2004**, *50*, 179.

(2) (a) Paul, F.; Lapinte, C. in Gielen, M.; Willem, R.; Wrackmeyer B., Eds. *Unusual Structures and Physical Properties in Organometallic Chemistry*; Wiley: New York, 2002; pp 220−291. (b) Tour, J. M. *Acc. Chem. Res.* **2000**, *33*, 791. (c) Paul, F.; Lapinte, C. *Coord. Chem. Rev.* **1998**, *178−180*, 431. (d) Ward, M. D. *Chem. Soc. Rev.* **1995**, *24*, 121. (e) Bunz, U. H. F. *Angew. Chem., Int. Ed. Engl.* **1994**, *33*, 1073. (f) Lang, H. *Angew. Chem., Int. Ed. Engl.* **1994**, *33*, 547. (g) Diederich, F.; Rubin, Y. *Angew. Chem., Int. Ed. Engl.* **1992**, *31*, 1101.

(3) (a) Kheradmandan, S.; Heinze, K.; Schmalle, H. W.; Berke, H. *Angew. Chem., Int. Ed.* **1999**, *38*, 2270. (b) Fernandez, F. J.; Blacque, O.; Alfonso, M.; Berke, H. *Chem. Commun*. **2001**, 1266. (c) Fernandez, F. J.; Venkatesan, K.; Blacque, O.; Alfonso, M.; Schmalle, H. W.; Berke, H. *Chem. Eur. J*. **2003**, *9*, 6192.

(4) (a) Brady, M.; Weng, W.; Zhou, Y.; Seyler, J. W.; Amoroso, A. J.; Arif, A. M.; Böhme, M.; Frenking, G.; Gladysz, J. A. *J. Am. Chem. Soc.* **1997**, *119*, 775. (b) Dembinski, R.; Lis, T.; Szafert, S.; Mayne, C. L.; Bartik, T.; Gladysz, J. A. *J. Organomet. Chem.* **1999**, *578*, 229. (c) Dembinski, R.; Bartik, T.; Bartik, B.; Jaeger, M.; Gladysz, J. A. *J. Am. Chem. Soc.* **2000**, *122*, 810.

(5) Akita, M.; Chung, M. C.; Sakurai, A.; Sugimoto, S.; Terada, M.; Tanaka, M.; Moro-oka, Y. *Organometallics* **1997**, *16*, 4882.

(6) (a) Le Narvor, N.; Toupet, L.; Lapinte, C. *J. Am. Chem. Soc.* **1995**, *117*, 7129. (b) Coat, F.; Lapinte, C. *Organometallics* **1996**, *15*, 477. (c) Coat, F.; Guillevic, M.-A.; Toupet, L.; Lapinte, C. *Organometallics* **1997**, *16*, 5988. (d) Le Narvor, N.; Lapinte, C. *C. R. Acad. Sci., Paris, Ser. IIC* **1998**, *1*, 745.

(7) Guillemot, M.; Toupet, L.; Lapinte, C. *Organometallics* **1998**, *17*, 1928.

10.1021/om050293a CCC: $30.25
Publication on Web 07/01/2005

tions revealing that the HOMOs of these complexes generally have both metal and carbon character, the relative amounts of which depend on the nature of the end-groups. Consequently, oxidation of these species can involve removal of electrons from orbitals that are delocalized over all atoms of the M−(C≡C)$_n$−M bridge[4a,8a] or from orbitals localized predominantly either on the carbon chain itself (as in the Mn complexes[3]) or at the metal centers (for Fe).[7] Calculations which have been carried out at various levels of theory reveal that the HOMO's of these polycarbon ligand complexes and their cations, although delocalized over the M−C$_4$−M backbone, are more metallic in character for examples containing first-row transition metals (except for Mn), whereas they possess greater carbon character in the examples featuring second and third row transition metals.

The still-puzzling magnetic properties of these redox-active complexes are directly linked to their electronic structures and are of considerable interest, both inherently and from the point of view of their potential applications. For example, while magnetic susceptibility measurements suggest a triplet ground state for the neutral complex with *trans*-MnI(dmpe)$_2$ end-caps (i.e., a neutral diradical with formal d^5−d^5 configurations at each Mn center), all other neutral M−C$_4$−M species described to date are diamagnetic and best described in terms of a buta-1,3-diyn-1,4-diyl structure (i.e., the limiting valence structure **A**, Scheme 1).[3] Sequential one-electron oxidations of the complex {*trans*-MnI(dmpe)$_2$}$_2$(μ-C≡CC≡C) lead to mono- and dications with doublet and singlet electronic structures, respectively, with the Mn centers capping an increasingly cumulenic carbon fragment.[3]

Some of the present authors have shown that the product derived from one-electron oxidation of {Fe(dppe)Cp*}$_2$(μ-C≡CC≡C) (**1**; Chart 1) also has a butadiyndiyl structure with the radical sites localized on the metal centers (structures **B**, **C**, Scheme 1). Further oxidation affords paramagnetic [**1**]$^{2+}$, with the singlet (**D**)−triplet (**E**) energy gap being sufficiently small (ΔG_{ST} = −18.2 cm^{-1}) for both states to be populated, even at liquid nitrogen temperatures. Removal of a third electron from the Fe−C$_4$−Fe substructure was also found to be possible, and the trication is isolable (as the PF$_6$ salt) when stabilized by the presence of very electron-donating and bulky dippe ligands, the complex salt [{Fe(dippe)Cp*}$_2$(μ-C$_4$)](PF$_6$)$_3$ ([**5**](PF$_6$)$_3$) being well described as a three-spin carrier at 293 K.[7]

The diruthenium complexes {Ru(PP)Cp′}$_2$(μ-C≡CC≡C) [Cp′ = Cp, PP = (PPh$_3$)$_2$ **2**; Cp′ = Cp*, PP = dppe **3**] can be readily oxidized to [**2**]$^{n+}$ or [**3**]$^{n+}$ (n = 1−4), with various spectroscopic, structural, and computational studies showing a smooth transition from the butadiyndiyl structure (**G**, Scheme 2) to the cumulenic structure **H** in the dications and eventually to the acetylide-bridged dicarbyne **I**.[8] Similar observations have been made for the rhenium complexes [{Re(NO)(PPh$_3$)Cp*}$_2$-

Scheme 1. Various Valence Bond Descriptions Which May Be Used to Describe the Oxidation of Compound 1

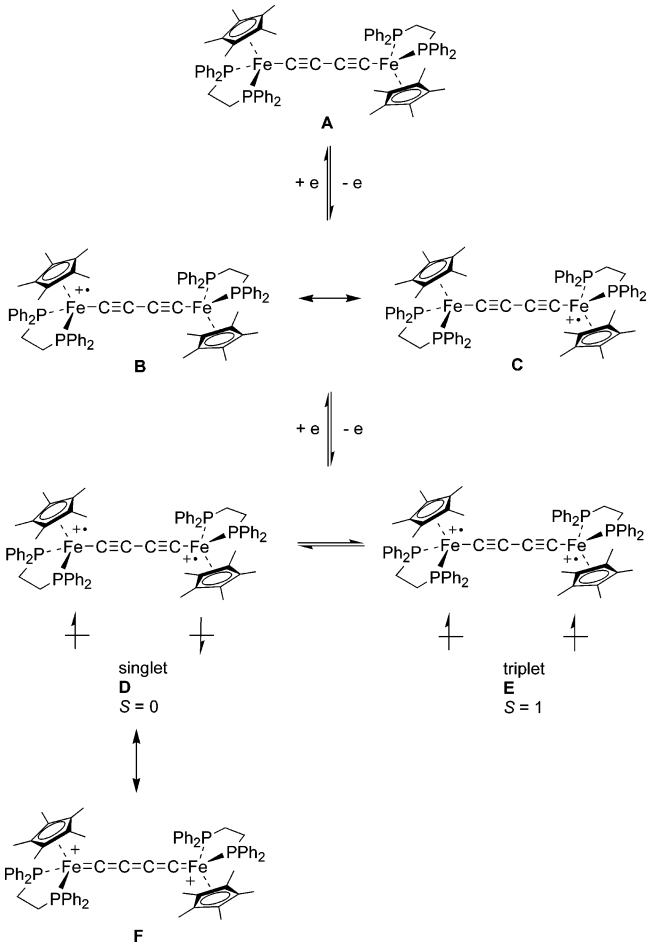

Chart 1

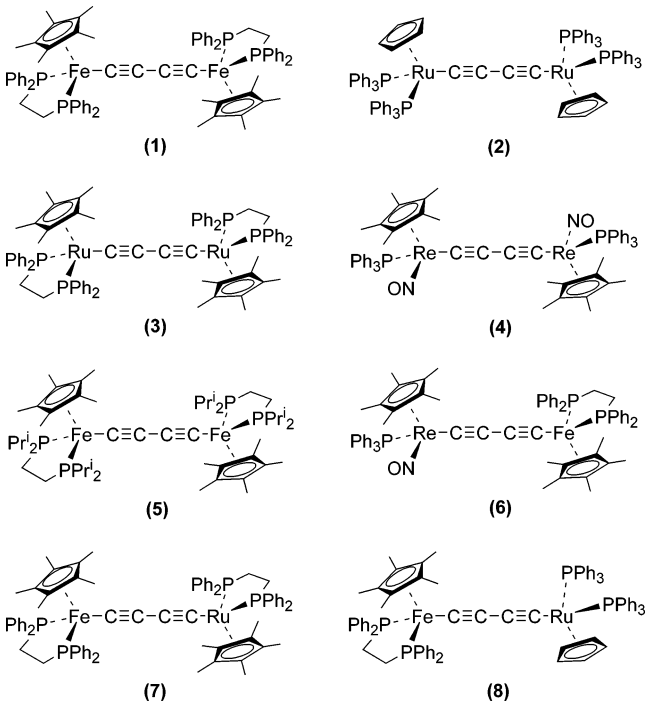

(μ-C$_4$)]$^{n+}$ (n = 0−2), although no dirhenium system of this type has yet been oxidized beyond the dication.[4] In contrast to the iron species [**1**]$^{2+}$, the dicationic ruthe-

(8) (a) Bruce, M. I.; Low, P. J.; Costuas, K.; Halet, J.-F.; Best, S. P.; Heath, G. A. *J. Am. Chem. Soc.* **2000**, *122*, 1949. (b) Bruce, M. I.; Ellis, B. G.; Low, P. J.; Skelton, B. W.; White, A. H. *Organometallics* **2003**, *22*, 3184. (c) Bruce, M. I.; Hall, B. C.; Kelly, B. D.; Low, P. J.; Skelton, B. K.; White, A. H. *J. Chem. Soc., Dalton Trans.* **1999**, 3719. (d) Bruce, M. I.; Kramarczuk, K. A.; Skelton, B. W.; White, A. H. Unpublished work.

Scheme 2. Valence Bond Descriptions Which May Be Used to Describe the Oxidation of Compounds 2 and 3[a]

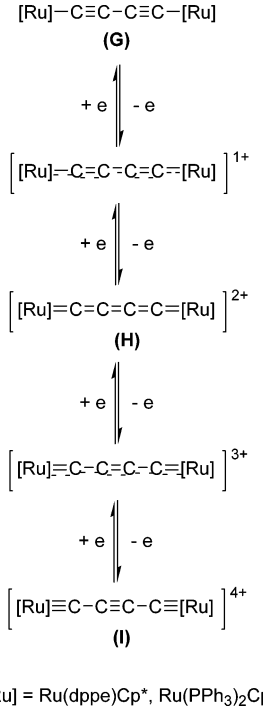

[a] Similar structures are appropriate for the oxidation of **4**.

nium and rhenium complexes $[\mathbf{2}]^{2+}$, $[\mathbf{3}]^{2+}$, and $[\mathbf{4}]^{2+}$ have been reported to be diamagnetic between 80 and 300 K.[8]

The families of complexes derived from **1** and **3** feature the same ligand environment about metal centers from the same periodic group, yet differ in terms of the number of accessible oxidation states and their electronic and magnetic structures. Given these structural similarities, the observed differences in magnetic and electronic behavior for the iron and ruthenium complexes suggest that it is the metal termini that play a decisive role in dictating the nature of the spin-carriers and their interactions, therefore underpinning the long-range magnetic and electronic interactions between them.

Efforts to explore further these structure/property relationships in poly-yndiyl complexes have resulted in the preparation of heterometallic species, including {Cp*(Ph$_3$P)(NO)Re}(C≡CC≡C){Fe(dppe)Cp*} (**6**).[9] The neutral heterodinuclear complex **6** is well described by the butadiyndiyl representation (**J**; Scheme 3) and can be oxidized to a monocation which exists in the ground state as an Fe-centered radical (**K**) but with low-lying, thermally and photochemically accessible higher energy states featuring a Re-centered radical (**L**). Further oxidation gives the dication, which shows a singlet/triplet equilibrium (**M/N**), for which the singlet can also be represented by the limiting form **O**. The singlet/triplet energy gap, ΔG_{ST}, is -175 cm^{-1}, the occupation of each state being 37/63 at 300 K.

However, as a result of the different electron counts and supporting ligands on Re and Fe, the end-caps are very different, which prevents a clear examination of the respective roles of the metals and ancillary ligands in determining the properties of these systems.

(9) Paul, F.; Meyer, W. E.; Toupet, L.; Jiao, H.; Gladysz, J. A.; Lapinte, C. *J. Am. Chem. Soc.* **2000**, *122*, 9405.

Scheme 3. Valence Bond Descriptions Associated with the Oxidation of 6

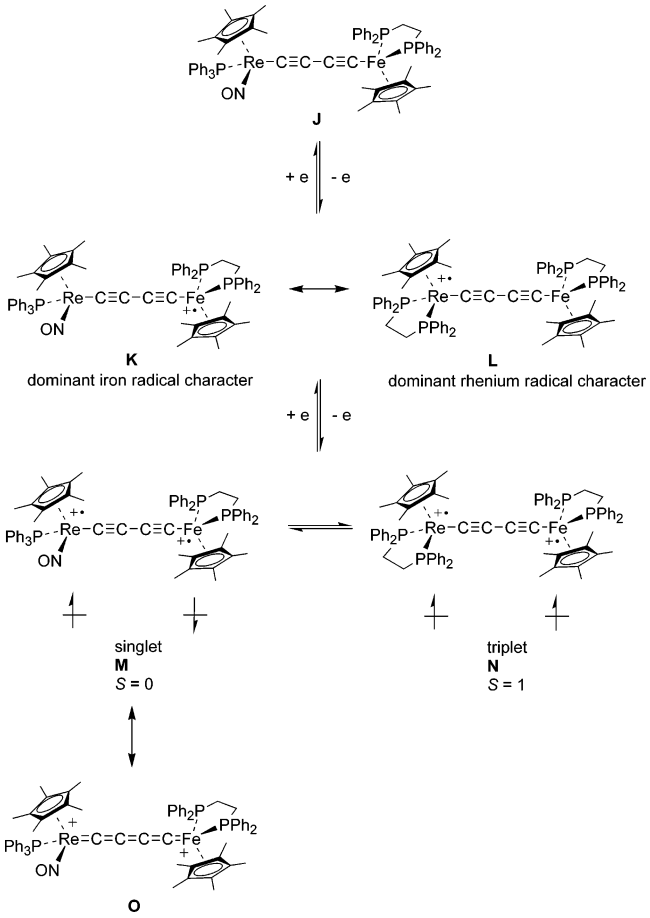

Thus it was of interest to examine the properties of mixed Fe−Ru diyndiyl complexes, which might be expected to exhibit behavior intermediate between those of **1**, **2**, and **3**, and **6**. The present paper gives a detailed account of the syntheses, spectroscopic, redox, and bonding properties of the mixed-metal complexes {Cp*(PP)Fe}(C≡CC≡C){Ru(PP′)Cp′} [PP = dppe, Cp′ = Cp*, PP′ = dppe, **7**; Cp′ = Cp, PP′ = $(PPh_3)_2$, **8**] and their oxidation products. Indeed, it was of particular interest (i) to prepare the mixed-metal Fe−Ru complex **7**, which differs from **1** and **3** only by replacement of an Fe or Ru atom by the other, and to examine the variations in physical properties induced by this nominally small change, and (ii) to explore the effect of replacement of the Cp* and dppe ligands at the Ru center by the less electron-releasing Cp and PPh_3 ligands on these properties, which might allow us to distinguish between the contributions arising from the change in metal center and those resulting from changes in the respective coordination spheres.

Results and Discussion

1. Syntheses and Characterization of 7 and 8. The ruthenium diynyls Ru(C≡CC≡CH)(dppe)Cp* (**9**) and Ru(C≡CC≡CH)$(PPh_3)_2$Cp (**10**)[10] were coupled with the iron-chloro precursor FeCl(dppe)Cp* in NEt_3 in the presence of Na[BPh_4] and dbu to give the heterobime-

Table 1. IR ν(CC) Modes (cm^{-1})[a]

complex	$n = 0$	$n = 1$	$n = 2$	ref
1	1955	1973	2160/1950	6
2	1970	1861	1760	8a
3	1966	1859	1769	8b
6	2093 (sh), 2058, 1955	2002, 1933, 1876	1941/1849/1783	9
7	1966	1986m (br), 1877	1870w, 1783s	this work
8	1965s (br)	1956 (br), 1883 (sh)	1890 (br), 1781m	this work
9	2166m, 2103s, 1997m			10
10	2165m, 2090s, 1980m			10
11	2107s, 1970 (br)			10
12	2109, 1971			
13	2171, 2095, 1990			10

[a] Nujol mulls; all weak unless otherwise stated.

Table 2. Selected ^{1}H, ^{13}C, and ^{31}P NMR Chemical Shifts (ppm)

	solvent	^{1}H Cp*	^{1}H Cp	^{13}C M*C*C	^{13}C MC*C*	^{31}P	ref
1	C_6D_6	1.55		99.7	110.2	101.9	6
[**1**]$(PF_6)_2$	d_8-toluene	−6.03				88.20, 89.91	6
2	C_6D_6		4.43			50.31	8a
[**2**]$(PF_6)_2$	d_6-acetone		5.03				8a
3	C_6D_6	1.68		94.63	99.47	82.53	8b
[**3**]$(PF_6)_2$	d_6-acetone	1.94				117.89	8b
7	$CDCl_3$	1.59[a]		100.75[a]	109.70[a]	101.90[a]	this work
		1.82[b]		93.57[b]	99.92[b]	82.55[b]	
[**7**]$(PF_6)_2$	d_6-acetone	−3.83[a]				291.83[a]	this work
		5.46[b]				51.24[b]	
8	$CDCl_3$	1.66	4.40			101.77[a]	this work
						52.43[b]	
[**8**]$(PF_6)_2$	$CDCl_3$	−0.86	5.05			86.24[a]	this work
						42.91[b]	

[a] Fe. [b] Ru.

Scheme 4. Synthesis of Compounds 7 and 8

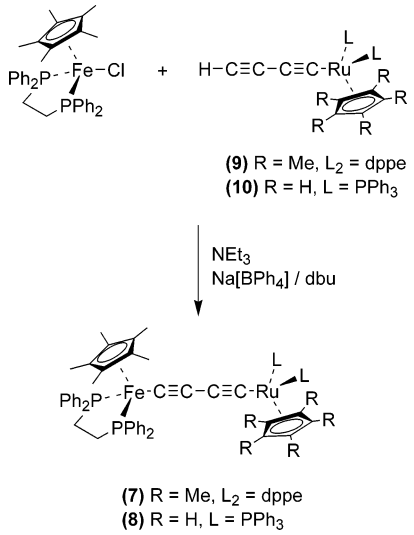

tallic complexes **7** and **8** in 70−80% yields (Scheme 4). For **8**, an equal volume of thf was required as a co-solvent because of the lower solubility of the starting diynyl **10**. The additional base dbu is essential for the efficient progress of the reaction, maximum yields of only ca. 50% being obtained in its absence. The lower yields suggest that equilibria exist between the neutral diyndiyls and their conjugate acids [{Cp*(PP)Fe}=C=CHC≡C{Ru(PP′)Cp′}]$^+$, the latter being formed by protonation of **7**−**9** by [$NHEt_3$]Cl.[11,12] The stronger base dbu enables the equilibrium to be driven in favor of the neutral complexes.

The mixed Fe−Ru diyndiyl complexes were readily identified from their IR and NMR spectra (Tables 1 and 2). Their expected diyndiyl nature is confirmed with ν(C≡C) bands found at ca. 1965 cm^{-1} in the Nujol mull spectra. Similar bands were also present in the homobimetallic complexes **1**−**3**. The ^{31}P NMR spectra of **7** and **8** confirm the presence of two different phosphorus nuclei in each of the complexes. In **7**, the resonances of the dppe ligands are at δ 101.90 and 82.55. For **8**, two broadened resonances of equal intensity were observed at δ 101.77 and 52.43. Comparisons with the spectra of **1**, **2**, and **3** permit the confident assignment of these resonances to the Fe- and Ru-bound ligands, respectively.

In the ^{1}H NMR spectra, the iron-bound Cp* methyl signals are generally close to δ 1.60, while resonances for the ruthenium-bound Cp* or Cp ligands are found at δ 1.82 and 4.40 for **7** and **8**, respectively. Other signals for the aromatic and CH_2 protons of the bidentate ligands are summarized in the Experimental Section, together with the ^{13}C resonances for the iron and ruthenium ML_x fragments. Unfortunately, resonances for the diyndiyl carbons were not observed at rt even with concentrated solutions. In one case, the spectrum of **7** in d_8-toluene was recorded at −80 °C, when broad resonances were found at δ 100.75 and 93.57, assigned to the Fe- and Ru-bound carbons, respectively. As shown in Table 2, these values compare well with those found in the symmetrical complexes **1**[6a] and **3**.[8b] The central carbons, C_2 and C_3, were observed at δ 109.70 and 99.92, respectively.

(10) Bruce, M. I.; Ellis, B. G.; Gaudio, M.; Lapinte, C.; Melino, G.; Paul, F.; Skelton, B. W.; Smith, M. E.; Toupet, L.; White, A. H. *Dalton Trans.* **2004**, 1601.

(11) (a) Bruce, M. I. *Chem. Rev.* **1991**, *91*, 197. (b) Bruce, M. I.; Swincer, A. G. *Adv. Organomet. Chem.* **1983**, *22*, 59.

(12) Bullock, R. M. *J. Am. Chem. Soc.* **1987**, *109*, 8087.

Table 3. Electrochemical Data for Various Complexes $\{ML_x\}C{\equiv}CC{\equiv}C\{M'L'_x\}$[a]

ML_x	E_1 (V)	E_2 (V)	E_3	E_4	$E_2 - E_1$	$E_3 - E_2$	$E_4 - E_3$	K_C/+1/+2	K_C/+2/+3	ref
(a) symmetrical										
$Mn(C{\equiv}CH)(dmpe)_2$	−0.451	+0.124			0.575			7.5×10^9	4.5×10^{10}	3
$Mn(C{\equiv}CSiMe_3)(dmpe)_2$	−0.816	−0.271			0.545			2.2×10^9		3
$Re(NO)(PPh_3)Cp^*$	0.01	0.54			0.53			1.1×10^9	9.2×10^8	4a
$Re(NO)[P(tol)_3]Cp^*$	−0.22	0.31			0.53			1.1×10^9	9.2×10^8	4c
$Fe(dppe)Cp^*$ (**1**)	−0.69	0.03	0.95		0.72	0.92		1.6×10^{12}	1.5×10^{11}	6
$Fe(dippe)Cp^*$ (**5**)	−0.97	−0.18	0.81		0.79	0.99		n/r	2.3×10^{13}	7
$Ru(PPh_3)_2Cp$ (**2**)	−0.23	0.41	1.03	1.68	0.64	0.62	0.65	1.5×10^{11}	6.6×10^{10}	8a
$Ru(PMe_3)(PPh_3)Cp$	−0.26	0.33	0.97	1.46	0.59	0.64	0.49	2.1×10^{11}	9.5×10^{10}	8a
$Ru(dppe)Cp^*$ (**3**)	−0.43	0.23	1.02	1.51[c]	0.66	0.79	0.49		1.4×10^{11}	8b
$Os(dppe)Cp^*$	−0.61	0.15	0.80	1.20	0.76	0.55	0.40		7.1×10^{12}	8d
(b) unsymmetrical										
$Re(NO)(PPh_3)Cp^*/Fe(dppe)Cp^*$ (**6**)	−0.50	0.23	1.33		0.73	1.10				9
$Fe(dppe)Cp^*/Ru(dppe)Cp^*$ (**7**)	−0.59	0.18	0.99		0.77	0.81				this work
$Fe(dppe)Cp^*/Ru(PPh_3)_2Cp$ (**8**)	−0.51	0.30	1.00		0.81	0.70				this work

[a] See individual papers for details of the electrochemical experiments. Data reported herein from 0.1 M $[NBu_4]PF_6/CH_2Cl_2$, scan rate 100 mV s^{-1}, 293 K, Pt electrodes.

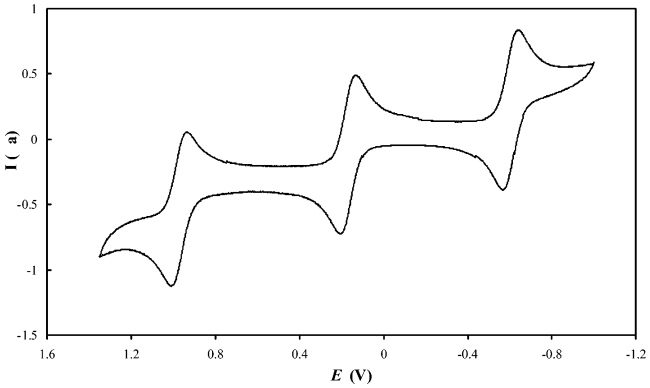

Figure 1. Cyclic voltammogram of **7** (0.1 M $[NBu_4]PF_6/CH_2Cl_2$, scan rate 100 mV s^{-1}, 293 K, Pt electrodes).

2. Electrochemistry. The cyclic voltammograms (CVs) of the Fe/Ru complexes **7** (Figure 1) and **8** show three chemically reversible waves separated by 0.77/0.81 and 0.81/0.70 V, respectively (Table 3). When measured under identical conditions, the CVs of the related monometallic complexes $M(C{\equiv}CC{\equiv}CR)(dppe)Cp^*$ [R = $SiMe_3$, M = Fe (**11**), Ru (**12**); R = H, M = Ru (**13**)] contained only one oxidation wave, which is fully reversible at iron and irreversible with ruthenium. The iron complex **11** is thermodynamically easier to oxidize than the ruthenium compounds [ΔE(**11**−**12**) = 0.44 and ΔE(**11**−**13**) = 0.58 V]. Comparison of the $E°$ values of the mononuclear complexes with those of the heterobinuclear derivatives shows that strong interactions exist between the end-groups in the latter ones. Specifically, substitution of the trimethylsilyl end-group in the iron complex **11** by a ruthenium end-group in **7** and **8** renders the oxidations 0.51/0.59 V more favorable.

Comparison of the $E°$ values of **7** and **8** with those of **1**, **2**, **3**, and **6** reveals the first oxidation process in **7/8** is 0.10/0.18 V less favorable than that in **1**. This suggests that substitution of an iron atom in **1** by a ruthenium atom in **7** or **8** decreases the energy of the HOMO. Interestingly, the second oxidation of **7/8** is more favorable than the first one in **11/12**. In the case of the third oxidation wave, the E values of **7** and **8** are very close to the data previously obtained for the related parent bis(iron) (**1**) and bis(ruthenium) (**2** and **3**) systems (Table 3). These oxidation potentials are far removed from the values obtained for the mononuclear derivatives and seem to be a characteristic feature of the electron-rich bimetallic systems. It is noteworthy that the fourth oxidation step observed for ruthenium complexes **2** and **3**, but not observed in the case of the iron complex **1**, is also not observed in the heterobimetallic derivatives **7** and **8** within the electrochemically accessible window.

3. Preparation of the Oxidized Complexes. Guided by the electrochemically determined oxidation potentials of **7** and **8**, the ferrocinium cation was chosen as oxidant for the preparation of the mono- and dicationic complexes. Addition of 0.95−1.0 molar equiv of $[FeCp^*_2]PF_6$ to solutions of the neutral complexes in CH_2Cl_2 resulted in immediate color changes from orange to dark brown. Workup gave the dark brown [**7**]PF_6 and [**8**]PF_6 in 91 and 96% yields, respectively. Treatment of [**7**]PF_6 or [**8**]PF_6 with a second equivalent of $[FeCp^*_2]PF_6$ in CH_2Cl_2, or reactions of **7** or **8** with 2 equiv of oxidant, gave dark blue [**7**]$(PF_6)_2$ and [**8**]$(PF_6)_2$ in 98 and 93% yields, respectively. As expected, both the mono- and dications give CVs that are identical with those of the neutral precursors **7** and **8**.

The current ratio of unity for the 2+/3+ oxidation process at the Pt electrode indicates that the tricationic species possesses some kinetic stability and suggested that it is a possible synthetic target. As the redox potential for the couples $[\mathbf{7}]^{2+}/[\mathbf{7}]^{3+}$ and $[\mathbf{8}]^{2+}/[\mathbf{8}]^{3+}$ are ca. +1.0 V (vs SCE), stronger oxidizing agents, such as $Ag[PF_6]$, were employed. However, all attempts to isolate the trications of **7** and **8** have so far been unsuccessful, with the products decomposing rapidly in solution, even at −78 °C. Nevertheless, it was possible to generate $[\mathbf{7}]^{3+}$ in an ESR tube and to obtain a well-resolved spectrum in a frozen CH_2Cl_2 glass (see ESR section).

4. Molecular Structures. As an aid to understanding the changes that occur upon oxidation, the molecular structures of **7**, [**7**]PF_6, [**7**]$(PF_6)_2$, **8**, and [**8**]PF_6 have been determined by single-crystal X-ray crystallography. On one occasion a crystal featuring a unit cell containing two cations derived from **8** and three PF_6^- anions was obtained, and the structure was successfully modeled in terms of a disordered mixture of [**8**]PF_6 and [**8**]$(PF_6)_2$. Details of this structure determination are given in the Supporting Information. Plots of molecules of **7** and **8** (as their CH_2Cl_2 solvates) are shown in Figure 2, while selected bond parameters are collected in Table 4. Table

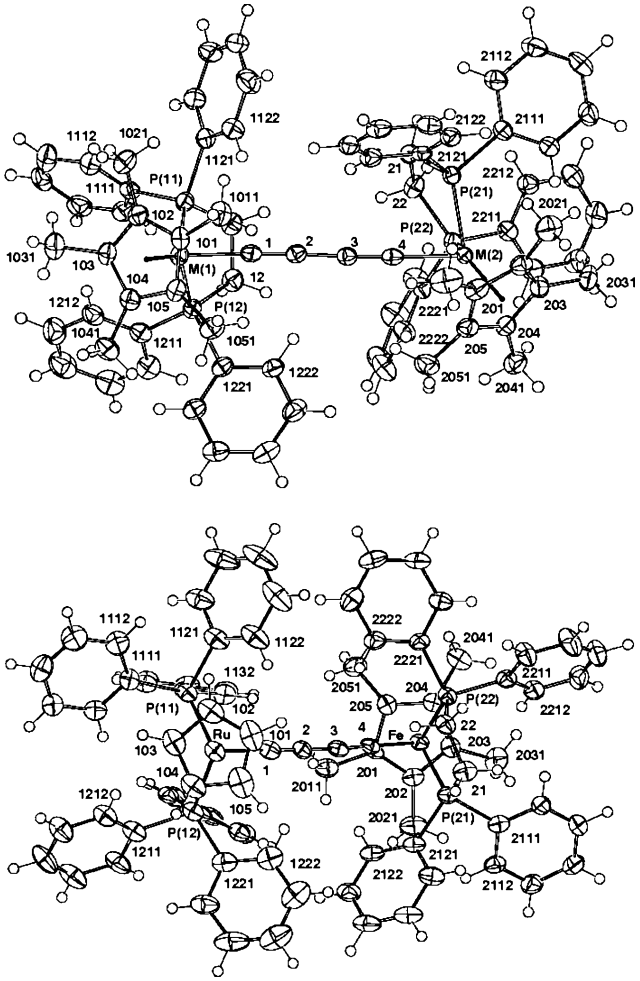

Figure 2. Plots of molecules of **7** (top) (Fe/Ru scrambled) and **8** (bottom).

5 compares the geometries of several related M−C_4−M fragments. In the crystals of its CH_2Cl_2 and benzene solvates, the metal sites in molecules of **7** are completely disordered, as are those in the cations $[\mathbf{7}]^{n+}$, perhaps not surprisingly because the ligand environments about the two metal centers are identical so that a distinction between the Fe and Ru centers is not possible. Consequently, the bond parameters measured are averages of the individual bond lengths and angles at the Fe and Ru centers.

As expected, the metal geometries are pseudo-octahedral and overall resemble those of other complexes containing the M(PP)Cp′ fragments [PP = $(PPh_3)_2$, dppe; Cp′ = Cp, Cp*]. However, considering the series $[\mathbf{7}]^{n+}$ (n = 0−2) and $[\mathbf{8}]^{n+}$ (n = 0, 1), several changes in individual bond lengths can be discerned as oxidation proceeds. Thus, as n increases, the M−P distances increase, consistent with a reduction in back-bonding from the metal center to the tertiary phosphine ligand. While the disorder prevents meaningful comparison of Fe−P and Ru−P bond lengths in the series derived from **7**, it is interesting to note the elongation of the Fe−P bond length in $[\mathbf{8}]^+$ vs **8** is ca. 2%, somewhat greater than the relative increase in the average Ru−P bond length (<0.5%) in the same complex. For complexes $[\mathbf{7}]^{n+}$, where the metal centers cannot be distinguished, only average values for the M−P and M−C distances can be compared. Nevertheless, as oxidation proceeds, the M−P separations increase to average values of 2.200(1), 2.25(1), and 2.30(1) Å for n = 0, 1, and 2, respectively. Oxidation also results in pronounced changes in the metrical parameters associated with the M−C_4−M chain. Within the family of complexes $[\mathbf{7}]^{n+}$ the M−C(1,4) bonds are 1.95(1) (n = 0), 1.886(2) (n = 1), and 1.83(1) Å (n = 2). The C≡C triple bonds lengthen from 1.23 through 1.24 to 1.26 Å, while the central C(2)−C(3) bond shortens from 1.374(6) through 1.349(3) to 1.325(5) Å. For neutral **8**, the Ru−C(1) and Fe−C(4) distances are 2.019 and 1.898(5) Å, respectively, which are typical separations for M−C(sp) single bonds and reflect the difference in atomic radii (Ru = 1.34, Fe = 1.26 Å).[13] In the monocations, shortening of the M−C distances to 1.953(5) (Ru) and 1.830(5) Å (Fe) is found, consistent with a considerable increase in the M−C bond order. The C(1)−C(2) and C(3)−C(4) separations, which in neutral **8** are the C≡C triple bonds, lengthen to 1.240(8) and 1.242(8) Å in the monocation, while the C(2)−C(3) bond contracts from 1.392(7) to 1.362(7) Å.

All these results are consistent with changes in the electronic structure of the M−C_4−M bridge which result in there being less electron density at the metal centers (less back-bonding from both metals to their phosphorus ligands, the effect being arguably more pronounced for the iron center than the ruthenium) and increases in the M−C and central C−C bond orders, with concomitant decreases in the C≡C triple bond order. These results are generally in accord with an earlier theoretical study of the homobimetallic Ru−C_4−Ru bridge and experimental results obtained for **2** and **3**.[8] Together these structural changes point to a change from the diynyl form **G** to the cumulenic structure **H** (Scheme 2) as the complex is oxidized.

As can be seen from Figure 2, the Fe−C_4−Ru linkages in the neutral complexes **7** and **8** are essentially linear with angles at individual carbons being in the small range 176.6−179.4(8)°. The total bending (Σ) is 11.1° and 7.6° for **7** and **8**, respectively, the chain adopting a *transoid* conformation with respect to the Cp* groups. After oxidation, deformation of the chain is somewhat greater (Σ = 32.8° and 34.7° for $[\mathbf{7}]^+$ and $[\mathbf{7}]^{2+}$ and 17.9° for $[\mathbf{8}]^+$). The related Fe/Re complex **6** shows a much larger bending in the chain, with angles at carbon between 169.6° and 176.6°.[9] As a consequence of the nonlinearity of the M−C_4−M moiety, in all cases the separations of the metal centers M···M′ lie between 7.5360(5) and 7.796(5) Å, necessarily shorter than the sums of the M−C and C−C distances.[14]

5. Theoretical Considerations. The results of a number of thorough computational studies examining the electronic and magnetic structures and bonding properties of C_4-containing bimetallic assemblies M−C_4−M have been reported.[3,4a,8a,9,15] To assess these parameters in the series of complexes described here, and to provide a comparison with those systems studied earlier, DFT studies have been carried out on systems chosen to model the redox series derived from **7** and **8**.

5.1. Molecular Geometries. To reduce computational effort, the hydrogen-substituted model heterobimetallic complexes [{Cp(dHpe)Fe}(μ-C_4){Ru(dHpe)Cp}]$^{n+}$, [**FeRu**]$^{n+}$ (dHpe = $PH_2CH_2CH_2PH_2$; n = 0−4),

(13) Shannon, R. P. *Acta Crystallogr.* **1976**, *A32*, 751.
(14) Szafert, S.; Gladysz, J. A. *Chem. Rev.* **2003**, *103*, 4175.

Table 4. Selected Bond Distances (Å) and Angles (deg)

	7·CH_2Cl_2	**7**·C_6H_6	[**7**]$^+$	[**7**]$^{2+}$	**8**	[**8**]$^+$
			Bond Lengths (Å)			
M(1)−P(11)	2.190(1)	2.1923(9)	2.2360(6)	2.239(7), 2.204(8)	2.289(2)	2.304(1)
M(1)−P(12)	2.201(1)	2.1999(8)	2.2680(6)	2.210(6), 2.333(8)	2.288(2)	2.295(1)
M(2)−P(21)	2.215(1)	2.2196(8)		2.396(11), 2.348(9)	2.168(2)	2.209(1)
M(2)−P(22)	2.197(1)	2.2049(8)		2.429(11), 2.206(9)	2.175(2)	2.228(2)
M(1)−C(cp)	2.141−2.201(4)	2.146−2.207(3)	2.172−2.227(2)	2.287−2.325(7), 2.156−2.305(10)	2.224−2.254(7)	2.231−2.263(6)
(av)	2.18(2)	2.18(2)	2.20(2)	2.30_1, 2.23_0	2.239(11)	2.247(12)
M(2)−C(cp)	2.155−2.214(4)	2.168−2.218(3)		2.090−2.212(9), 2.081−2.237(10)	2.100−2.144(5)	2.130−2.159(5)
(av)	2.18(2)	2.20(2)		2.15_5, 2.15_8	2.12(2)	2.140(12)
M(1)−C(1)	1.939(4)	1.932(3)	1.886(2)	1.881(7), 1.731(9)	2.019(5)	1.953(5)
C(1)−C(2)	1.223(6)	1.228(5)	1.240(3)	1.261(5)	1.226(7)	1.240(8)
C(2)−C(3)	1.374(6)	1.386(5)	1.349(3)	1.325(5))	1.392(7)	1.362(7)
C(3)−C(4)	1.233(6)	1.220(4)		1.260(5)	1.238(7)	1.242(8)
C(4)-M(2)	1.957(4)	1.965(4)		1.908(10), 1.808(10)	1.898(5)	1.830(5)
M(1)···M(2)	7.721(1)	7.7262(6)		7.5360(7)	7.768(1)	7.594(1)
			Bond Angles (deg)			
P(11)−M(1)−P(12)	83.05(4)	82.87(3)	83.21(2)	84.5(3), 86.4(2)	101.49(6)	99.82(5)
P(11)−M(1)−C(1)	85.1(1)	85.0(1)	84.11(7)	93.7(4), 83.8(2)	87.6(2)	88.1(2)
P(12)−M(1)−C(1)	82.3(1)	82.76(9)	93.66(7)	86.3(3), 96.2(3)	85.5(2)	91.3(1)
P(21)−M(2)−P(22)	84.04(4)	83.99(3)		84.1(3), 78.3(4)	85.77(7)	85.12(5)
P(21)−M(2)−C(4)	81.6(1)	81.74(9)		84.8(4), 80.2(4)	84.1(2)	86.8(2)
P(22)−M(2)−C(4)	82.5(1)	82.14(9)		86.0(3), 91.9(4)	84.6(2)	87.0(2)
M(1)−C(1)−C(2)	177.3(4)	177.5(3)	166.1(2)	171.7(4), 169.2(4)	178.3(5)	175.9(5)
C(1)−C(2)−C(3)	176.6(4)	177.1(3)	177.5(3)	174.0(4)	177.4(7)	176.1(5)
C(2)−C(3)-C(4)	177.7(4)	177.9(4)		173.3(4)	177.3(6)	177.4(6)
C(3)−C(4)−M(2)	177.3(4)	177.5(3)		170.8(4), 164.2(5)	179.4(5)	172.7(5)
∑ (total bend)	11.1	10.0	32.8	34.7	7.6	17.9

Table 5. Bond Parameters for Several [{L_xM}−C−C−C−C−{$M'L'_y$}]$^+$ Complexes

$ML_x/M'L'_y$	n	M−C(1)/ M′−C(4)	C(1)−C(2)	C(2)−C(3)	C(3)−C(4)	M−C(1)−C(2)/ M′−C(4)−C(3)	C(1)−C(2)−C(3)	C(2)−C(3)−C(4)	ref
(a) symmetrical									
MnI(dmpe)$_2$	0	1.798(15)	1.263(17)	1.33(3)		176.1	177.4	177.4	3
MnI(dmpe)$_2$	1	1.763(2)	1.275(3)	1.313(5)		179.1	179.3		3
MnI(dmpe)$_2$	2	1.768, 1.770(4)	1.289(5)	1.295(5)	1.298(5)				3
Re(NO)(PPh$_3$)Cp*	0	2.037(5)	1.202(7)	1.389(5)		174.4(5)	176.8(6)		4a
Re(NO)(PPh$_3$)Cp*	2	1.909, 1.916(7)	1.263(10)	1.305(10)		168.5/171.4(7)	177.8(9)	175.4(9)	4a
Fe(dppe)Cp*	0	1.885, 1.889(9)	1.22(1)	1.37(1)	1.22(1)	175(1)/179(1)	177(1)	176(1)	15
Fe(dppe)Cp*	1	1.830(8)	1.236(9)	1.36(1)		167.0(6)	177(1)		6a
Fe(dippe)Cp*	3	1.79(1)	1.27(1)	1.33(1)		175.2(9)	178.7(9)		7
Ru(dppe)Cp*	0	2.007, 2.016(8)	1.22(1)	1.40(1)	1.22(1)	177.1(9)/171.4(9)	176(1)	172(1)	8b
Ru(dppe)Cp*	1	1.931(2)	1.248(3)	1.338(3)		165.6(2)	178.0(2)		8b
Ru(dppe)Cp*	2	1.856, 1.858(5)	1.280(7)	1.294(7)	1.269(7)	175.6(5)/170.1(4)	176.7(6)	174.2(6)	8b
Ru(PPh$_3$)$_2$Cp	0	2.001(3)	1.217(4)	1.370(6)		178.9(2)	177.2(3)		8c
Os(dppe)Cp*	0	2.010, 2.015(3)	1.220(4)	1.380(4)	1.224(4)	177.4(3)/177.2(3)	176.2(3)	177.3(3)	8d
(b) unsymmetrical									
Re(NO)(PPh$_3$)Cp*/ Fe(dppe)Cp*	0	2.029(6)/ 1.895(6)	1.209(8)	1.370(9)	1.224(9)	176.6(5)/169.6(6)	178.3(7)	177.4(7)	9
Fe(dppe)Cp*/ Ru(dppe)Cp*	0	1.932(3)/ 1.965(4)	1.228(5)	1.386(5)	1.220(4)	177.5(3)/177.5(3)	177.1(3)	177.9(4)	this work
Fe(dppe)Cp*/ Ru(PPh$_3$)$_2$Cp	0	1.898(5)/ 2.019(5)[a]	1.226(7)	1.392(7)	1.238(7)	178.3(5)/179.4(5)	177.4(7)	177.3(6)	this work

[a] Values for Fe−C(4)/Ru−C(1).

were used to mimic compound **7** and were first optimized at the DFT level of theory (see computational details). In the interests of internal consistency in the data, similar calculations were also conducted on [{Cp(dHpe)Fe}$_2$(μ-C_4)]$^{n+}$, [**Fe$_2$**]$^{n+}$ (n = 0−4), and [{Cp(dHpe)Ru}$_2$(μ-C_4)]$^{n+}$, [**Ru$_2$**]$^{n+}$ (n = 0−4), as models for the real compounds **1** and **3**, respectively, for comparative purposes. Salient structural parameters are given in Table 6. A comparison of the metrical parameters computed for [**Fe$_2$**] and [**Ru$_2$**] with the corresponding bond lengths and bond angles of the crystallographically characterized **1**−**3** reveals good agreement, allowing some confidence with respect to the reliability of the computational methods employed. We note, in common with previously reported computational studies,[4a,8a] a 2−3% overestimate in the M−C and C−C bond lengths. Because of the Fe/Ru disorder in **7**, comparisons between the structural parameters computed for model [**FeRu**] are best made against **8**, where again excellent agreement is observed. As measured experimentally, the two

Table 6. Pertinent Optimized Bond Lengths (Å), Relative Energies (E_{rel}, eV), and Adiabatic Ionization Potentials (IP, eV) for Models $[Ru_2]^{n+}$, $[Fe_2]^{n+}$, $[FeRu]^{n+}$ ($n = 0-4$), $[Re_2]^{n+}$ and $[FeRe]^{n+}$ ($n = 0-2$)[a]

complex	M−C(α)	C(α)−C(β)	C(β)−C(β′)	C(β′)−C(α′)	M′− C(α′)	M−P	M′−P	M−C(Cp)	M′−C(Cp)	E_{rel}	IP
[Ru$_2$]	2.035	1.242	1.367	1.243	2.038	2.268	2.266	2.338	2.344		4.97
3[b]	2.001(3)	1.223(4)	1.382(4)	1.218(4)	2.003(3)						
[Ru$_2$]$^+$	1.968	1.261	1.332	1.261	1.967	2.297	2.298	2.346	2.347		8.39
[3]$^+$[b]	1.931(2)	1.248(3)	1.338(3)	1.248(3)	1.931(2)						
[Ru$_2$(S)]$^{2+}$	1.919	1.277	1.311	1.278	1.920	2.330	2.329	2.351	2.350	0	11.76
[Ru$_2$(T)]$^{2+}$	1.906	1.284	1.307	1.283	1.909	2.342	2.340	2.353	2.346	+0.13	
[3]$^{2+}$[b]	1.858(5)	1.280(7)	1.338(3)	1.269(7)	1.856(5)						
[Ru$_2$]$^{3+}$	1.873	1.301	1.287	1.302	1.871	2.378	2.372	2.353	2.355		15.19
[Ru$_2$]$^{4+}$	1.836	1.331	1.268	1.330	1.836	2.421	2.403	2.371	2.385		
[Fe$_2$]	1.913	1.246	1.365			2.164		2.133			4.79
1[c]	1.889(9)	1.22(1)	1.37(1)	1.22(1)	1.885(8)						
[Fe$_2$]$^+$	1.851	1.259	1.339			2.190		2.142			8.40
[1]$^+$[c]	1.830(8)	1.236(9)	1.36(1)	1.236(9)	1.830(8)						
[Fe$_2$(S)]$^{2+}$	1.796	1.276	1.314			2.225		2.158		0	11.75
[Fe$_2$(T)]$^{2+}$	1.794	1.279	1.313			2.233		2.167		−0.01	
[Fe$_2$]$^{3+}$	1.747	1.300	1.289			2.268		2.176			15.44
[Fe$_2$]$^{4+}$	1.708	1.332	1.267			2.311		2.198			
[FeRu]	1.925	1.246	1.370	1.244	2.043	2.150	2.263	2.138	2.353		4.83
[FeRu]$^+$	1.848	1.261	1.339	1.261	1.973	2.180	2.293	2.153	2.347		8.40
[FeRu(S)]$^{2+}$	1.796	1.278	1.316	1.279	1.923	2.214	2.330	2.163	2.352	0	11.75
[FeRu(T)]$^{2+}$	1.790	1.282	1.310	1.284	1.922	2.214	2.327	2.165	2.349	+0.04	
[FeRu]$^{3+}$	1.742	1.301	1.288	1.302	1.875	2.251	2.362	2.179	2.361		15.28
[FeRu]$^{4+}$	1.708	1.332	1.269	1.334	1.838	2.296	2.408	2.200	2.381		
[Re$_2$]	2.077	1.243	1.360	1.243	2.076	2.399	2.398	2.383	2.384		5.34
14[d]	2.037(5)	1.202(7)	1.389(5)			2.375(1)					
[Re$_2$]$^+$	2.023	1.260	1.332	1.260	2.023	2.429	2.426	2.399	2.400		8.85
[Re$_2$(S)]$^{2+}$	1.974	1.279	1.307	1.279	1.975	2.470	2.469	2.402	2.403	0	
[Re$_2$(T)]$^{2+}$	1.990	1.277	1.312	1.276	1.991	2.481	2.492	2.400	2.399	+0.43	
[14]$^{2+}$[d]	1.909(7)	1.263(10)	1.305(10)	1.260(10)	1.916(7)	2.439(2)	2.430(2)				
[FeRe]	1.899	1.247	1.360	1.245	2.083	2.166	2.399	2.134	2.390		5.09
15[e]	1.895(6)/Fe	1.209(8)	1.370(9)	1.224(9)	2.029(6)/Re	2.175[f]	2.353(2)				
[FeRe]$^+$	1.841	1.261	1.334	1.258	2.025	2.196	2.426	2.155	2.403		8.62
[FeRe(S)]$^{2+}$	1.799	1.280	1.310	1.279	1.973	2.224	2.461	2.157	2.405	0	
[FeRe(T)]$^{2+}$	1.796	1.275	1.315	1.272	1.993	2.236	2.466	2.169	2.398	+0.18	

[a] Crystallographic data for corresponding complexes are given when available. [b] Reference 8. [c] Reference 6. [d] Reference 4. [e] Reference 9. [f] Average.

C≡C triple bond lengths in the model complex [**FeRu**] are nearly identical, 1.246 vs 1.244 Å, indicating that the unsymmetrical nature of the complex introduces hardly any polarization in the ground state. The same conclusion was drawn from related dirhenium and iron−rhenium systems according to calculations carried out earlier at the B3LYP hybrid density functional level of theory on the complexes {Cp(NO)(PH$_3$)Re}$_2$(μ-C$_4$) [**Re$_2$**] and {Cp(dHpe)Fe}(μ-C$_4$){Re(NO)(PH$_3$)Cp} [**FeRe**], which are models for {Cp*(NO)(PPh$_3$)Re}$_2$(μ-C$_4$) (**4**) and {Cp*(dppe)Fe}(μ-C$_4$){Re(NO)(PPh$_3$)Cp*} (**6**), respectively.[15] For comparative purposes and for the sake of consistency with the complexes discussed here, calculations on these two models [**Re$_2$**] and [**FeRe**] were performed again at the BP86 density functional level of theory. Pertinent structural parameters are given in Table 6. In all neutral complexes considered, the distances are consistent with a buta-1,3-diyn-1,4-diyl electronic structure.

The electron counts of the model systems [**Fe$_2$**], [**Ru$_2$**], [**Re$_2$**], [**FeRu**], and [**FeRe**] were each reduced by one and two electrons to mimic the effects of oxidation, and the structures were optimized. The results obtained were compared to corresponding X-ray data where available (see Table 6). The computational models confirm the trend observed experimentally, i.e., a decrease in the lengths of the M−C and C−C single bonds and an increase in the C≡C triple bond lengths upon oxidation. This is accompanied by a notable elongation of the metal−phosphorus bond distances in each case. Of particular interest are the geometries of the dicationic species, which can exhibit different spin configurations. Notably, calculations do not indicate significant differences between the bond separations optimized for the singlet state and triplet state configurations, and similar M−C and C−C bond separations are computed for high- and low-spin configurations for both homo- and heterobimetallic complexes (Table 6). Consequently, although the computed structures mirror rather well the corresponding experimentally characterized dicationic species, bond analyses of the crystallographically characterized dicationic complexes are insufficient to assign their magnetic configurations. Regardless of the spin state, the computed outer and central C−C bonds show a degree of alternation in diiron [**Fe$_2$**]$^{2+}$ and iron−ruthenium [**FeRu**]$^{2+}$ species that is slightly greater than in the diruthenium [**Ru$_2$**]$^{2+}$ species (Table 6). Nevertheless, these C−C bond lengths are sufficiently close to each other in all of the dicationic species to consider that the cumulenic valence formulation is dominant overall in the description of their electronic distribution.

5.2. Energy Decomposition of the M−C Bond in C$_4$-Containing Bimetallic Complexes. Metal−carbon interactions in different C$_4$-containing bimetallic complexes were investigated with an energy partitioning analysis (EPA).[16] The advantage of this approach is to estimate the interaction energy (ΔE_{int}) between the

(15) Jiao, H.; Costuas, K.; Gladysz, J. A.; Halet, J.-F.; Guillemot, M.; Toupet, L.; Paul, F.; Lapinte, C. *J. Am. Chem. Soc.* **2003**, *125*, 9511.

(16) (a) Morokuma, K. *J. Chem. Phys.* **1971**, *55*, 1236. (b) Ziegler, T.; Rauk, A. *Theor. Chim. Acta* **1977**, *46*, 1.

Table 7. Computed Hirshfeld Charges and Dipole Moments for Models $[Ru_2]^{n+}$, $[Fe_2]^{n+}$, $[FeRu]^{n+}$, $[FeRe]^{n+}$, and $[Re_2]^{n+}$ (n = 0, 2)

complex	M	C(α)	C(β)	C(β′)	C(α′)	M′	∑MC$_4$M	μ_D[a]
[**Ru$_2$**]	+0.22	−0.21	−0.12	−0.12	−0.21	+0.21	−0.23	0.22
[**Ru$_2$(S)**]$^{2+}$	+0.29	−0.12	−0.03	−0.03	−0.12	+0.29	+0.28	
[**Ru$_2$(T)**]$^{2+}$	+0.29	−0.10	−0.02	−0.02	−0.10	+0.29	+0.29	
[**Fe$_2$**]	−0.05	−0.17	−0.12	−0.12	−0.17	−0.05	−0.68	0.03
[**Fe$_2$(S)**]$^{2+}$	+0.01	−0.09	−0.03	−0.03	−0.09	+0.01	−0.22	
[**Fe$_2$(T)**]$^{2+}$	+0.01	−0.08	−0.03	−0.03	−0.08	+0.01	−0.20	
[**FeRu**]	−0.06/Fe	−0.17	−0.11	−0.12	−0.21	+0.22/Ru	−0.45	1.05
[**FeRu(S)**]$^{2+}$	−0.01	−0.08	−0.02	−0.02	−0.11	+0.30	+0.06	
[**FeRu(T)**]$^{2+}$	−0.01	−0.07	−0.01	−0.01	−0.09	+0.29	+0.10	
[**FeRe**]	−0.05/Fe	−0.16	−0.11	−0.11	−0.19	+0.12/Re	−0.50	2.64
[**FeRe(S)**]$^{2+}$	0.01	−0.07	−0.02	+0.01	−0.10	+0.23	+0.06	
[**FeRe(T)**]$^{2+}$	+0.03	−0.08	−0.01	−0.02	−0.09	+0.21	+0.04	
[**Re$_2$**]	+0.13	−0.18	−0.10	−0.10	−0.18	+0.13	−0.30	4.04
[**Re$_2$(S)**]$^{2+}$	+0.23	−0.09	−0.00	−0.00	−0.09	+0.23	+0.28	
[**Re$_2$(T)**]$^{2+}$	+0.23	−0.08	−0.00	−0.00	−0.08	+0.23	+0.18	

[a] Dipole moment (Debye).

metal centers and the carbon atoms as the sum of the energy contributions of the stabilizing orbital interactions (ΔE_{orb}), the attractive metal carbon electrostatic contributions (ΔE_{elst}), and repulsion interactions (ΔE_{Pauli}) (see the Experimental Section). The heterolytic approach [2 M^+ + $(C_4)^{2-}$] was chosen for the analysis.

Comparison of the ΔE_{int} values computed for the different complexes indicates that the M−C bond is slightly stronger in [**Fe$_2$**] than in [**Ru$_2$**] and [**FeRu**] (−20.08, −19.64, and −19.67 eV, respectively). The covalent character (ΔE_{orb}) is nearly equal in the homodinuclear complexes (−9.64 and −9.60 eV for [**Fe$_2$**] and [**Ru$_2$**], respectively). Less covalent character is computed for the heterodimetallic species [**FeRu**] (−9.22 eV). On the other hand, the steric repulsion (ΔE_{Pauli}) is larger for the diruthenium species than for the diiron and the mixed iron−ruthenium complexes (20.87, 20.05, and 19.24 eV, respectively). Note that a stronger attractive electrostatic interaction is computed for [**Ru$_2$**] (−30.92 eV) than for either [**Fe$_2$**] (−30.48 eV) or [**FeRu**] (−29.69 eV).

5.3. Population Analysis and Dipole Moments. Table 7 shows the atomic net charges for several complexes obtained using the Hirshfeld analysis.[17] In all neutral complexes, the carbon atoms are negatively charged. Interestingly, the total negative charge of the C_4 link is nearly constant regardless of the attached metal atoms, suggesting that the supporting Cp and phosphine ligands are involved in supplying charge to the polycarbon chain. As perhaps would be expected, the iron centers are calculated to be electron-rich relative to the ruthenium and rhenium centers. The different metal and carbon charges in the heterobimetallic species establish somewhat polarized structures (Table 7), an observation that is confirmed by the computed dipole moments, which are also good descriptors of the ground-state total charge distribution. The dipole moments computed for [**Fe$_2$**] and [**Ru$_2$**] differ slightly from zero, as a consequence of the lack of a center of symmetry in these computational models (Table 7). A larger dipole moment perpendicular to the ReC_4Re backbone is computed for [**Re$_2$**] due the particular orientation of the NO groups. Larger dipole moments are calculated for the heterometallic species, amounting to 1.05 and 2.64 D for [**FeRu**] and [**FeRe**], respectively, with the negative end at Fe for the former and at Re for the latter because of the NO group tethered to it. Computed atomic net charges for low-spin and high-spin dicationic species are also reported in Table 7. Their evolution indicates that both metal and carbon atoms lose electron density upon oxidation, in accord with the X-ray data.

5.4. Spin Configurations. While the calculated molecular geometries of the singlet and triplet electronic states of $[Ru_2]^{2+}$ are similar, energetically the singlet state [**Ru$_2$(S)**]$^{2+}$ is largely favored by 0.13 eV (12.8 kJ mol^{-1}) compared to the triplet state [**Ru$_2$(T)**]$^{2+}$. In contrast, the energies computed for the triplet state [**Fe$_2$(T)**]$^{2+}$ and the singlet state [**Fe$_2$(S)**]$^{2+}$ are equal, being separated by less than 0.01 eV (1 kJ mol^{-1}) in favor of the high-spin configuration, a value that is within the limits of accuracy of the method used. For the mixed iron−ruthenium species, the low-spin configuration [**FeRu(S)**]$^{2+}$ is now 0.04 eV (4 kJ mol^{-1}) more stable than the high-spin configuration [**FeRu(T)**]$^{2+}$. The computed singlet−triplet energy gaps in the series [**Fe$_2$**]$^{2+}$ (−1 kJ mol^{-1}), [**FeRu**]$^{2+}$ (+4 kJ mol^{-1}), and [**Ru$_2$**]$^{2+}$ (+12.8 kJ mol^{-1}) are less pronounced than those calculated for the series [**Fe$_2$**]$^{2+}$ (−1 kJ mol^{-1}), [**FeRe**]$^{2+}$ (+17.3 kJ mol^{-1}), and [**Re$_2$**]$^{2+}$ (+41.3 kJ mol^{-1}), providing computational support for the idea that the electronic configuration (high spin vs low spin) strongly depends on the metal.

5.5. Spin Densities. Atomic spin densities were computed for different open-shell systems in order to probe the delocalization of the unpaired electron(s). According to the computed values given in Table 8, the unpaired electron of the monocationic homobimetallic species is extensively distributed over the overall M−C_4−M backbone. Nevertheless, the metal vs carbon spin density populations depend on the nature of the metal atoms. For [**Ru$_2$**]$^+$, the single electron is located less at the ruthenium atoms than on the C_4 chain (0.352 vs 0.562). Inversely, a greater portion of the spin density in [**Fe$_2$**]$^+$ is found associated with the iron atoms than with the carbon atoms of the C_4 bridge (0.650 vs 0.398). In the heterobimetallic species [**FeRu**]$^+$ the spin density on iron is nearly twice that on ruthenium (0.290 vs 0.166), consistent with the more electron-donating character of the iron entity and leading to a polarized structure. Similar behavior is also noted for the hetero-

(17) (a) Hirshfeld, F. L. *Theor. Chem.* **1977**, *44*, 129. (b) Bickelhaupt, F. M.; van Eikema Hommes, N. J. S.; Guerra, C. F.; Baerends, E. J. *Organometallics* **1996**, *15*, 2923.

Table 8. Mulliken Atomic Spin Densities for the Open-Shell Models $[Ru_2]^{n+}$, $[Fe_2]^{n+}$, $[Re_2]^{n+}$, $[FeRu]^{n+}$, and $[FeRe]^{n+}$ (n = 1, 2)

complex	M	C(α)	C(β)	C(β′)	C(α′)	M′	M_2	C_4
[Ru$_2$]$^+$	0.176	0.175	0.106	0.106	0.175	0.176	0.352	0.562
[Fe$_2$]$^+$	0.325	0.115	0.084	0.084	0.115	0.325	0.650	0.398
[Re$_2$]$^+$	0.250	0.155	0.101	0.101	0.155	0.249	0.499	0.512
[FeRu]$^+$	0.290/Fe	0.157	0.092	0.103	0.163	0.166/Ru	0.456	0.515
[FeRe]$^+$	0.364/Fe	0.125	0.097	0.087	0.144	0.223/Re	0.587	0.453
[Ru$_2$(T)]$^{2+}$	0.390	0.336	0.213	0.213	0.336	0.386	0.776	1.098
[Fe$_2$(T)]$^{2+}$	0.634	0.245	0.173	0.173	0.245	0.635	1.269	0.836
[Re$_2$(T)]$^{2+}$	0.412	0.280	0.178	0.177	0.281	0.420	0.832	0.916
[FeRu(T)]$^{2+}$	0.602/Fe	0.302	0.181	0.209	0.313	0.369/Ru	0.971	1.005
[FeRe(T)]$^{2+}$	0.776/Fe	0.174	0.212	0.133	0.287	0.369/Re	1.145	0.806

bimetallic **[FeRe]**$^+$ (0.364 vs 0.223). Interestingly, the spin populations on the metal atoms in these heterobimetallic species are similar to the corresponding values in the homobimetallic complexes.

Atomic spin density calculations also reveal highly delocalized systems for the high-spin dicationic species. In the cases of **[Ru$_2$(T)]**$^{2+}$ and **[Re$_2$(T)]**$^{2+}$ the spin density is spread slightly less over the two metal centers than over the carbon linkage (0.776 vs 1.098 in the former and 0.832 vs 0.916 in the latter). In contrast, the spin density is more localized on the metal atoms than at the carbon ligand (1.269 vs 0.836) in the iron species **[Fe$_2$(T)]**$^{2+}$. Intermediate metal vs carbon distribution values are computed for the heterobimetallic compounds **[FeRu(T)]**$^{2+}$ and **[FeRe(T)]**$^{2+}$ (0.971 vs 1.005 and 1.145 vs 0.806, respectively). As with the heterobimetallic monocations, in both cases the highest spin population is found on iron, roughly twice that on ruthenium or rhenium (Table 8). This suggests that the high-spin states of these dicationic structures are also highly polarized.

5.6. Molecular Orbitals. As noted previously, molecular orbital (MO) patterns of neutral C_4-containing complexes show closely spaced HOMO and HOMO−1, which result from four-electron repulsive π-type interactions between metal and carbon chain frontier orbitals. Consequently, these frontier orbitals, which are M−C(α) and C(β)−C(β′) antibonding and C(α)−C(β) bonding, are delocalized over the M−C_4−M backbone, as illustrated for **[FeRu]** in Figure 3. Analysis of the energy and composition of the HOMO and HOMO−1 within the series of homo- and heterobimetallic M−C_4−M systems as a function of the metal allows further information to be obtained concerning the nature of the metal-to-carbon chain bonding. To this end, a Mulliken atomic orbital population analysis for different neutral complexes is given in Table 9. Examination of the metal vs carbon percentage contribution to the HOMO and HOMO−1 reveals that the replacement of Fe by Ru yields MOs less heavily weighted on the metal. In **[Ru$_2$]** the HOMO contains 26% metal and 62% C_4 character, whereas the HOMO−1 is 21% metal and 69% C_4 in character. Corresponding values for **[Fe$_2$]** are 41% metal and 46% carbon and 36% metal and 52% carbon, respectively. In the mixed species **[FeRu]** the HOMO and HOMO−1 feature a more important contribution on Fe than on Ru (18 vs 12% and 15 vs 9%, respectively). Interestingly, the participation of the C_4 linker, which is 57 and 67% in the HOMO and HOMO−1, respectively, is evenly distributed on C(α) (17 and 21%) and C(α′) (18 and 22%) and on C(β) (11 and 12%) and C(β′) (11 and 12%).

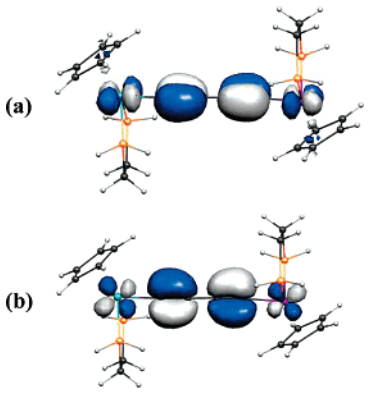

Figure 3. HOMO (a) and HOMO−1 (b) calculated for **[FeRu]** (Ru at left, Fe at right). Contour values are ±0.045 (e/bohr^3)$^{1/2}$.

Although the compositions of the HOMO and HOMO−1 may not be significantly altered upon oxidation and must remain essentially delocalized over the M−C_4−M linkage, it is important to look at the nodal properties of these orbitals computed for the singlet (LUMO and HOMO) and triplet (SOMOs) dicationic species. Their energy and composition are given in Table 9. A small increase in the amount of metal character and a corresponding decrease in the C_4 content result from removal of electrons. For instance, the metal character percentage increases from 26 and 21% in the neutral **[Ru$_2$]** species for the HOMO and HOMO−1 to 36 and 33% in the dicationic singlet **[Ru$_2$(S)]**$^{2+}$ complex for the corresponding LUMO and HOMO, respectively. A smaller increase is computed in the diiron species with a shift from 41 and 36% in the neutral **[Fe$_2$]** to 44 and 40% in the singlet **[Fe$_2$(S)]**$^{2+}$, respectively. In the case of the heterodinuclear complex **[FeRu]**, a significant increase of the metal contribution is also observed during the progression from the neutral to singlet dicationic complexes (30 and 23% vs 39 and 35%). It is also noteworthy that the iron character in these MOs increases more readily with respect to the ruthenium character upon oxidation (Ru/Fe ratio: 0.67 and 0.60 for the neutral complex vs 0.86 and 0.75 for the singlet dicationic model).

We may wonder if there is any relationship between the preferred spin configuration of the dicationic species and the HOMO−LUMO gap found for the singlet ground state; that is, the higher the HOMO−LUMO gap, the more stable the low-spin state. In the series **[Ru$_2$(S)]**$^{2+}$, **[FeRu(S)]**$^{2+}$, and **[Fe$_2$(S)]**$^{2+}$, the HOMO−LUMO gap shifts slightly from 0.24 to 0.20 to 0.20 eV. A larger shift is computed in the series **[Re$_2$(S)]**$^{2+}$, **[FeRe(S)]**$^{2+}$, and **[Fe$_2$(S)]**$^{2+}$ (from 0.68 to 0.43 to 0.20

Table 9. Energies (eV) and Mulliken Decomposition (%) of the HOMO and HOMO−1 of the Models $[Ru_2]^{n+}$, $[Fe_2]^{n+}$, $[Re_2]^{n+}$, $[FeRu]^{n+}$, and $[FeRe]^{n+}$ (n = 0, 2)[a]

complex	MO	energy/eV	M	C(α)	C(β)	C(β′)	C(α′)	M′	M_2	C_4
[**Ru$_2$**]	HOMO	−3.07	13	19	12	12	19	13	26	62
	HOMO−1	−3.32	11	22	12	12	23	10	21	69
[**Fe$_2$**]	HOMO	−3.11	21	13	10	10	13	20	41	46
	HOMO−1	−3.41	18	16	10	10	16	18	36	52
[**Re$_2$**]	HOMO	−3.581	16	17	10	10	17	16	32	54
	HOMO−1	−4.19	3	22	11	11	22	3	6	66
[**FeRu**]	HOMO	−3.00	18/Fe	17	11	11	18	12/Ru	30	57
	HOMO−1	−3.26	15/Fe	21	12	12	22	9/Ru	23	67
[**FeRe**]	HOMO	−3.51	20/Fe	15	10	10	15	18/Re	38	50
	HOMO−1	−3.60	32/Fe	11	14	5	17	1/Re	33	47
$[Ru_2(S)]^{2+}$	LUMO	−9.67	18	11	10	10	11	18	36	42
	HOMO	−9.91	17	18	11	11	18	16	33	58
$[Fe_2(S)]^{2+}$	LUMO	−9.78	22	11	10	10	11	22	44	42
	HOMO	−9.98	20	15	11	11	15	20	40	52
$[Re_2(S)]^{2+}$	LUMO	−10.24	19	11	10	10	11	19	38	42
	HOMO	−10.92	6	17	10	10	17	6	12	54
[**FeRu(S)**]$^{2+}$	LUMO	−9.71	21/Fe	12	9	10	11	18/Ru	39	42
	HOMO	−9.91	20/Fe	16	11	11	17	15/Ru	35	55
[**FeRe(S)**]$^{2+}$	LUMO	−10.01	22/Fe	11	9	10	11	18/Re	40	41
	HOMO	−10.44	24/Fe	13	13	7	18	5/Re	29	51
$[Ru_2(T)]^{2+}$	SOMO	−9.90(↑)/−9.85(↓)	19(↑)/17(↓)	10(↑)/17(↓)	9(↑)/11(↓)	9(↑)/11(↓)	10(↑)/17(↓)	19(↑)/16(↓)	38(↑)/33(↓)	38(↑)/56(↓)
	SOMO−1	−10.41(↑)/-9.45(↓)	20(↑)/19(↓)	15(↑/12(↓)	11(↑)/10(↓)	11(↑)/10(↓)	15(↑)/12(↓)	19(↑)/19(↓)	39(↑)/38(↓)	52(↑)/44(↓)
$[Fe_2(T)]^{2+}$	SOMO	−10.00(↑)/-9.35(↓)	21(↑)/24(↓)	11(↑)/9(↓)	10(↑)/9(↓)	10(↑)/9(↓)	11(↑)/9(↓)	21(↑)/24(↓)	42(↑)/48(↓)	42(↑)/36(↓)
	SOMO−1	−10.45(↑)/-9.76(↓)	18(↑)/20(↓)	15(↑)/14(↓)	11(↑)/11(↓)	11(↑)/11(↓)	15(↑)/14(↓)	18(↑)/20(↓)	36(↑)/40(↓)	52(↑)/50(↓)
$[Re_2(T)]^{2+}$	SOMO	−10.67(↑)/-10.40(↓)	17(↑)/17(↓)	10(↑)/11(↓)	8(↑)/8(↓)	8(↑)/8(↓)	10(↑)/12(↓)	17(↑)/16(↓)	34(↑)/33(↓)	36(↑)/39(↓)
	SOMO−1	−11.02(↑)/-10.52(↓)	17(↑)/16(↓)	11(↑)/12(↓)	8(↑)/8(↓)	8(↑)/8(↓)	11(↑)/12(↓)	18(↑)/18(↓)	35(↑)/34(↓)	38(↑)/40(↓)
[**FeRu(T)**]$^{2+}$	SOMO	−9.95(↑)/−9.81(↓)	17(↑)/23(↓)	12(↑)/11(↓)	7(↑)/9(↓)	11(↑)/10(↓)	9(↑)/11(↓)	22(↑)/18(↓)	39(↑)/41(↓)	39(↑)/41(↓)
	SOMO−1	−10.43(↑)/-9.42(↓)	17(↑)/21(↓)	16(↑)/15(↓)	9(↑)/11(↓)	12(↑)/11(↓)	15(↑)/17(↓)	21(↑)/14(↓)	38(↑)/35(↓)	50(↑)/54(↓)
[**FeRe(T)**]$^{2+}$	SOMO	−10.52(↑)/-9.98(↓)	12(↑)/18(↓)	15(↑)/12(↓)	5(↑)/7(↓)	14(↑)/11(↓)	7(↑)/10(↓)	32(↑)/27(↓)	40(↑)/41(↓)	44(↑)/40(↓)
	SOMO−1	−10.78(↑)/-10.11(↓)	19(↑)/34(↓)	10(↑)/6(↓)	12(↑)/13(↓)	6(↑)/4(↓)	16(↑)/14(↓)	6(↑)/3(↓)	23(↑)/44(↓)	41(↑)/37(↓)

[a] The HOMO and HOMO−1 of the neutral species become the LUMO and HOMO of the singlet dicationic species and the SOMO and SOMO−1 of the triplet dicationic species.

eV, respectively). Clearly, HOMO−LUMO gaps for the low-spin dicationic systems are related, although not linearly, to the stability of the low-spin vs high-spin configurations.

5.7. Ionization Potentials. The adiabatic ionization potentials (IPs) computed for different complexes are compared in Table 6. The diiron species [**Fe$_2$**] is more readily ionized than its diruthenium counterpart [**Ru$_2$**] (e.g., 4.79 vs 4.97 eV for the first IP), reflecting the more electron-donating nature of the iron end-group. An intermediate value, 4.83 eV, is computed for the heterobimetallic derivative [**FeRu**], consistent with the delocalized nature of these systems. This clearly indicates that IPs are strongly dependent on the nature of the metal centers since the ligand surroundings are the same for all of these three complexes. Not surprisingly, [**Re$_2$**], which contains less electron-releasing ancillary ligands, is more difficult to oxidize, with a first IP of 5.34 eV. Interestingly, the solution-phase oxidation potentials track rather well these computed gas-phase IPs since the cyclic voltammetry data show the same trend, i.e., the ease of $E_1(0/1+)$ oxidation being

1 (−0.69 V) > **7** (−0.59 V) > **6** (−0.50 V) > **3** (−0.43 V) > **4** (+0.01 V)

6. IR Spectroscopy. The IR spectra of the cationic complexes $[\mathbf{7}]^{n+}$ and $[\mathbf{8}]^{n+}$ show two ν(CC) bands, suggesting that the symmetry of the complexes decreases as the oxidation proceeds (Table 1). This finding is also consistent with increased polarization of the M−C_4−M′ axis in the oxidation products (see ESR and Mössbauer sections). The frequencies decrease with oxidation, consistent with a gradual reduction in CC bond order (Table 1). The two vibrational modes observed in $[\mathbf{7}]^{n+}$ and $[\mathbf{8}]^{n+}$ (n = 1, 2) can probably be assigned to the Ru−CC and Fe−CC stretching modes, respectively. Nevertheless, comparisons with the data obtained for the homobinuclear families of complexes $[\mathbf{1}]^{n+}$ and $[\mathbf{2/3}]^{n+}$ suggest that the changes in the structure of the C_4 chain in the $[\mathbf{Fe/Ru}]^{n+}$ complexes are not as marked as those found in $[\mathbf{2}]^{n+}$, although they are more pronounced than those in $[\mathbf{1}]^{n+}$. The IR spectra of both $[\mathbf{7}]^{2+}$ and $[\mathbf{8}]^{2+}$ suggest that the carbon chain structures in these dications lie between the diyndiyl and cumulenic structures in accord with the computed carbon−carbon distances (Table 6).

7. ^{57}Fe Mössbauer Spectroscopy. Mössbauer spectroscopy is a very sensitive probe that can be used to identify the electronic environment of an iron nucleus.[18] The quadrupole splitting (QS) and isomer shift (IS) can provide insight into the nature of the bonds formed from ligands to iron: for example, previous studies in the Fe(dppe)Cp* series have shown characteristic values of QS for alkyl-Fe(II) (2.0 mm s^{-1}), alkyl-Fe(III) (0.90 mm s^{-1}), and carbene-Fe(II) complexes (1.2 mm s^{-1}).[19] The ^{57}Fe Mossbauer spectra of the series $[\mathbf{7}]^{n+}$ and $[\mathbf{8}]^{n+}$ (n = 0−2) were measured at 80 K. At zero field, the spectra of these complexes all show unique doublets; the fitting parameters for these are summarized in Table 10 and compared with values obtained for related complexes.

The IS values of the neutral mixed-metal complexes **6**−**8** listed in Table 10 are slightly smaller than those of the bis(iron) derivative **1** and some related acetylide

(18) Gütlich, P.; Link, R.; Trautwein, A. *Mössbauer Spectroscopy and Transition Metal Chemistry*; Springer: Berlin, 1978; Vol. 3.

(19) Le Stang, S.; Paul, F.; Lapinte, C. *Organometallics* **2000**, *19*, 1035.

Table 10. ^{57}Fe Mössbauer Fitting Parameters (80 K)

compound	IS/mm s^{-1}	QS/mm s^{-1}	γ/mm s^{-1}	ref
1	0.27	2.07		6
[**1**]PF_6	0.21	1.32		
[**1**]$(PF_6)_2$	0.18	1.05		
6	0.255	1.983	0.130	9
[**6**]PF_6	0.191	0.995	0.194	
[**6**]$(PF_6)_2$	0.138	0.957	0.146	
7	0.252	2.006	0.139	this work
[**7**]PF_6	0.211	1.147	0.167	
[**7**]$(PF_6)_2$	0.151	1.113	0.135	
[**7**]$(PF_6)_2$ (273 K)	0.177	1.069	0.130	
8	0.260	1.966	0.152	this work
[**8**]PF_6	0.225	0.983	0.272	
[**8**]$(PF_6)_2$	0.167	0.931	0.156	
9	0.293	2.066	0.125	this work
[**9**]PF_6	0.156	1.114	0.250	

complexes.[20] As the IS value is related to the electron density at the iron nucleus, it can therefore be assumed that the electron density on the iron center is similar for all three mixed-metal complexes, consistent with the delocalized electronic structures calculated using DFT methods. This conclusion is further corroborated by the redox potentials. The QS values determined for the neutral complexes are typical of Fe(II) complexes of this type and compare well with the data in Table 10.

In the case of the monocations [**7**]$^+$ and [**8**]$^+$, the IS values are significantly smaller than in the corresponding neutral complexes, indicating that the iron center is strongly affected by the oxidation of the molecule. In these two complexes, the electronic density at the iron nucleus is close to that determined for the bis(iron) mixed-valence complex [**1**]$^+$, as shown by the comparison of the IS values (Table 10). The QS values found for the cations [**7**]$^+$ (1.147 mm s^{-1}) and [**8**]$^+$ (0.983 mm s^{-1}) are outside the range of values usually found in oxidized acetylide complexes [Fe(C≡CR)(dppe)Cp*]$^+$ (0.846−0.90 mm s^{-1}), suggesting that the unpaired electron is probably delocalized on the whole [Fe]−C_4−[Ru] linkage, and in keeping with this suggestion the iron nucleus is best described as having an oxidation state that is between 2 and 3. The spin densities computed from the model compound [**FeRu**]$^+$ show that the unpaired electron is less localized on the iron nucleus than on the RuC_4 fragment (0.29 vs 0.68), which is consistent with the Mössbauer observations.

The decrease of the IS values when the monocations [**7**]$^+$ and [**8**]$^+$ are oxidized to the dications indicates that the second oxidation leads to a further diminution of the electronic density at the iron nucleus. Previous results obtained with different diradical bis(iron) complexes of the Fe(dppe)Cp* series indicate that the QS parameters should be different in the triplet and in the singlet states (0.8 vs 1.1 mm s^{-1}).[19−22] In the case of [**7**]$^{2+}$, the QS value at 273 K is much smaller than the value measured at 80 K, in accord with thermal population of the triplet excited state. There is no further change in the magnitude of QS upon cooling of the sample to 4 K, suggesting that the limiting (triplet) structure is obtained at ca. 80 K, at least in the solid state. The observation of a unique doublet at room temperature demonstrates that the exchange rate between the two spin isomers is fast enough to give an averaged signal on the Mössbauer time scale (ca. 10^{-8} s).

Table 11. ESR Parameters[a]

compound	g_1	g_2	g_3	g_{iso}[b]	Δg[c]	ref
[**1**]PF_6	2.139	2.089	2.079	2.102	0.060	13
[**1**]$(PF_6)_2$	*d*					
[**3**]PF_6	2.2284	2.0697	1.9910	2.096	0.232	
[**6**]PF_6	2.2356	2.0075	1.9292	2.054	0.315	20
[**6**]$(PF_6)_2$	2.04	2.10	2.15			
[**7**]PF_6	2.1865	2.0820	1.9995	2.089	0.187	31
[**7**]$(PF_6)_2$	*d*					
[**7**]$(PF_6)_3$	2.3655	2.0565	1.9770	2.133	0.388	
[**8**]PF_6	2.2820	2.0542	1.9890	2.108	0.293	
[**8**]$(PF_6)_2$	*d*					

[a] 80 K, CH_2Cl_2/CH_2ClCH_2Cl (1/1) glass. [b] $g_{iso} = (g_1 + g_2 + g_3)/3$. [c] $\Delta g = g_1 - g_3$. [d] ESR silent.

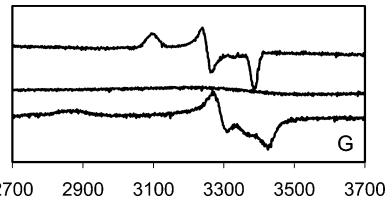

Figure 4. ESR spectra of [**7**]PF_6 (top), [**7**]$(PF_6)_2$ (medium), and [**7**]$(PF_6)_3$ (bottom) at 80 K (in CH_2Cl_2/CH_2ClCH_2Cl).

8. ESR Spectroscopy. To probe their electronic structures in more detail, the X-band ESR spectra of the various cations obtained from **7** and **8** were recorded at 80 K in CH_2Cl_2/CH_2ClCH_2Cl (1/1 v/v) glasses, and the details are summarized in Table 11, which also includes data for similar species from **1** and **3**. The spectra of [**7**]$(PF_6)_n$ (n = 1−3) are shown in Figure 4. The spectra of the mono- and trications display three features corresponding to the three components of the g tensor expected for a pseudo-octahedral d^5 low-spin Fe(III) complex.[2c,19−22] No hyperfine coupling between the unpaired electron and phosphorus was observed. The dication in [**7**]$(PF_6)_2$ is ESR silent at 77 K both as a powder and in solution. At 293 K, a very broad and weak signal was observed (g = 2.009).

Direct determination of the isotropic g (g_{iso}) values for the monocations was not possible since these complexes are not ESR-active at temperatures above the melting points of the solvents. The calculated g_{iso} values for [**3**]$^+$, [**7**]$^+$, and [**8**]$^+$ are close to the values obtained for the related radicals [**1**]$^+$ and [**6**]$^+$.[6,9] The g_{iso} value found for [**3**]$^+$ is slightly smaller than g_{iso} determined for the corresponding bis(iron) derivative, in agreement with an increased carbon character of the HOMO in the bis(ruthenium) series.[8a] The small variations in g_{iso} found for [**7**]$^+$ and [**8**]$^+$ are consistent with expectations based on the varying degrees of electron density at the different metal centers. The smaller g_{iso} found for [**7**]$^+$ (slightly smaller than for [**3**]$^+$) suggests that the SOMO which contains the unpaired electron has increased ruthenium and carbon character; that is, the system is delocalized and the more electron-rich Ru(dppe)Cp* moiety in [**7**]$^+$ is effectively coupled to the iron center through the C_4 bridge. In contrast, cation [**8**]$^+$ has a larger g_{iso} value (slightly larger than [**1**]$^+$), which suggests a greater degree of iron character in the

(20) Denis, R.; Toupet, L.; Paul, F.; Lapinte, C. *Organometallics* **2000**, *19*, 4240.
(21) Argouarch, G.; Thominot, P.; Paul, F.; Toupet, L.; Lapinte, C. *C. R. Chim.* **2003**, *6*, 209.
(22) Roué, S.; Le Stang, S.; Toupet, L.; Lapinte, C. *C. R. Chim.* **2003**, *6*, 353.

SOMO. The ESR spectrum is therefore consistent with a model for $[\mathbf{8}]^+$ in which there is a greater contribution from the valence structure $RuC{\equiv}CC{\equiv}CFe^{+\bullet}$ than is the case for $[\mathbf{7}]^+$. Similar conclusions can also be drawn from the relative magnitudes of the IS and QS parameters in the Mössbauer experiments.

It has already been suggested that in a homogeneous series of mixed-valence (MV) compounds the anisotropy tensor of the ESR signal ($\Delta g = g_1 - g_3$) decreases as the rate of the intramolecular electron transfer increases.[23,24] For example, Δg values are much larger in the trapped MV complex [1,3-{Cp*(dppe)FeCC}$_2$C$_6$H$_4$]-PF_6 ($\Delta g = 0.530$)[25] than in the detrapped MV isomer [1,4-{Cp*(dppe)FeCC}$_2$C$_6$H$_4$]PF_6 ($\Delta g = 0.168$)[26] and in the highly delocalized [**1**]PF_6 ($\Delta g = 0.060$).[6a] The *g*-tensor anisotropy of $[\mathbf{3}]^+$ is larger than that of its bis(iron) homologue $[\mathbf{1}]^+$. However, if we assume that in a family of nonsymmetrical MV compounds all having the same electron-rich end-cap, i.e., Fe(dppe)Cp*, the smaller the *g*-tensor anisotropy, the greater the directional intramolecular electron transfer, it can be suggested that the rate of electron transfer decreases in the order $[\mathbf{7}]^+ > [\mathbf{8}]^+ > [\mathbf{6}]^+$.

In an attempt to observe the triplet state, the X-band ESR spectra of $[\mathbf{7}]^{2+}$ and $[\mathbf{8}]^{2+}$ were also recorded at different temperatures in the range 4−80 K, both in a CH_2Cl_2/CH_2ClCH_2Cl (1/1 v/v) glass and using powdered samples. Only weak broad signals around $g = 2$ were found in some spectra obtained from the powders. The $\Delta m_s = 2$ transition characteristic of the triplet state was not observed, in contrast with the bis(iron) dications and the related Fe/Re dication.[9,15] Magnetic susceptibility measurements were also carried out from 2 to 300 K with crystalline samples of $[\mathbf{7}]^{2+}$. A linear variation of the product ΔT vs T was found in the range 50−300 K. Determination of the singlet−triplet energy gap by the variation of the magnetic susceptibility with temperature was precluded by a large temperature-independent paramagnetism term (TIP) diagnostic of the presence of adventitious traces of paramagnetic impurities formed during the crystal-growing process. In this particular case, however, the determination of the singlet/triplet energy gap by VT paramagnetic ^{1}H and ^{31}P NMR was more successful (see below).

The trication $[\mathbf{7}]^{3+}$ was prepared in situ by adding a small amount (0.5−0.7 equiv) of $[FeCp_2]PF_6$ to a CH_2Cl_2/CH_2ClCH_2Cl solution of the ESR-silent dication $[\mathbf{7}]^{2+}$ at 193 K, whereupon the blue solution immediately turned black. The solution was immediately frozen at 80 K and an ESR spectrum was run. A well-resolved spectrum with three tensor components was obtained. However, after warming the sample at 293 K for 3 min and then cooling again to 80 K, a second spectrum of $[\mathbf{7}]^{3+}$ showed a significant decrease of the signal intensity, suggesting that this complex does not constitute a viable synthetic target. As shown in Table 11, the ESR parameters of $[\mathbf{7}]^{3+}$ are completely different from those of the monocation $[\mathbf{7}]^+$. It is also noteworthy that the spectrum of $[\mathbf{7}]^{3+}$ is completely different from that of $[\mathbf{5}]^{3+}$, for which a quartet electronic structure was proposed on the basis of ESR and magnetic susceptibility data,[7] and in agreement with DFT calculations.[15] In contrast, the small line width of the signal components observed in the ESR spectrum of $[\mathbf{7}]^{3+}$ suggests that this complex should have a single unpaired electron in the ground state ($S = 1/2$). The large g_{iso} and Δg values are in agreement with a strong metallic character for the SOMO in $[\mathbf{7}]^{3+}$. This is in full agreement with the DFT calculations, which indicates that the spin density in the trication $[\mathbf{FeRu}]^{3+}$ is more localized on the iron atom than in the corresponding monocation (0.36 vs 0.29) and less on the ruthenium center (0.17 vs 0.14).

9. ^{1}H Paramagnetic NMR Studies. Only broad resonances were observed in the NMR spectra of $[\mathbf{7}]PF_6$ and $[\mathbf{8}]PF_6$, confirming their paramagnetic nature. The strong antiferromagnetic interaction, which precludes recording their ESR spectra (see above), favors observation of well-resolved NMR spectra of the dications, although the resonances are shifted with respect to those of the neutral complexes, as expected for paramagnetic compounds. Table 2 compares the ^{1}H NMR spectra of $[\mathbf{7}]^{2+}$ and $[\mathbf{8}]^{2+}$ with those of the symmetrical analogues $[\mathbf{1}]^{2+}$ and $[\mathbf{3}]^{2+}$, all as the PF_6 salts. The most notable features are the shifts in the ^{1}H and ^{13}C resonances of the Cp′ ligands: compared with the neutral complexes, the Fe−Cp* resonances shift upfield, while the Ru−Cp signals move downfield. Similar relative shifts are also observed with the symmetrical complexes, in which the Fe−Cp* resonances associated with $[\mathbf{1}]^{2+}$ move upfield relative to **1** (although to a greater extent), while the Ru−Cp protons in $[\mathbf{3}]^{2+}$ are shifted downfield relative to the resonances in **3**. The ^{31}P signals also follow this trend, with the dppe ligand on Fe shifted downfield and the PPh_3 ligands on Ru shifted upfield. In $[\mathbf{7}]^{2+}$, the two resonances for the dppe ligands are ca. 80 and 210 times broader than the PF_6 resonances ($w_{1/2} = 27$ Hz) and clearly show the paramagnetic nature of the complex. Assuming that the line broadening depends on the spin density on the metal centers, the signal at δ −51.2 can be assigned to the Ru-dppe ligand, whereas the broader signal at δ 289.8 is assigned to the Fe-dppe ligand.

For paramagnetic compounds, the observed isotropic shift may arise from contact and/or dipolar interactions (eq 1):[28]

$$\delta_{obs} = \delta_{iso} + \delta_{dia} = \delta_{contact} + \delta_{dipolar} + \delta_{dia} \qquad (1)$$

For simple mononuclear systems with one unpaired electron ($S = 1/2$), both contact and dipolar terms are expected to have an inverse temperature dependence, but for compounds with $S > 1/2$, the zero-field splitting can also lead to dipolar shift with a T^{-2} temperature dependence.[29] The presence of simultaneous contact and dipolar contributions to the observed isotropic shifts can be established by detection of curvature in a Curie

(23) Rieger, P. H. *Coord. Chem. Rev.* **1994**, *135−136*, 203.
(24) (a) Dong, T.-Y.; Sohel, C.-C.; Hwang, M.-Y.; Lee, T. Y.; Yeh, S.-K.; Wen, Y.-S. *Organometallics* **1992**, *11*, 573. (b) Dong, T.-Y.; Hendrickson, D.; Pierpont, C. G.; Moore, M. F. *J. Am. Chem. Soc.* **1986**, *108*, 963.
(25) Weyland, T.; Costuas, K.; Toupet, L.; Halet, J.-F.; Lapinte, C. *Organometallics* **2000**, *19*, 4228.
(26) Le Narvor, N.; Lapinte, C. *Organometallics* **1995**, *14*, 634.
(27) Kahn, O. *Molecular Magnetism*; VCH: New York, 1993; Chapter 6.
(28) Bertini, I.; Luchinat, C. *NMR of Paramagnetic Molecules in Biological Systems*; Benjamin/Cummings: Menlo Park, 1986.
(29) Wicholas, M.; Mustacich, R.; Jayne, D. *J. Am. Chem. Soc.* **1972**, *94*, 4518.

plot.[30] The observed isotropic shifts were plotted against $1/T$ for compounds containing two ($S = 1$) and three ($S = 3/2$) $[Fe(dppe)Cp^*]^+$ units, and in both cases linear relationships were found,[31] indicating that the Curie law is obeyed in this family of compounds and the isotropic shift is essentially contact in origin. Independent magnetic susceptibility measurements have shown that the ground and excited states are close enough in energy to be statistically populated at 80 K.[31] In that case the singlet/triplet ratio remained unchanged in the temperature range accessible for NMR measurements in solution. However, for compounds in which the singlet/triplet energy gaps are larger, population of the ground state can significantly increase as the temperature decreases, thereby inducing a deviation from the Curie law. The variation of the magnetic susceptibility, χ, is given by eq 2, which is derived from the Van Vleck equation:[27,28,32]

$$\chi = C/T[3 + \exp(-J/kT)] \qquad (2)$$

Variable-temperature ^{1}H NMR spectra were obtained for [**7**]$(PF_6)_2$ and [**8**]$(PF_6)_2$. As has been shown for monomeric 17-electron complexes in the Fe(dppe)Cp* series, the presence of the unpaired electron predominantly affects the chemical shifts of the methyl groups of the Cp* ligands,[33] so we have focused our attention on the chemical shifts of the Cp* ligands coordinated to both the iron (δ_{Cp^*Fe}) and ruthenium (δ_{Cp^*Ru}) centers. In accord with a singlet ground state for both [**7**]$(PF_6)_2$ and [**8**]$(PF_6)_2$, one finds that all the resonances move toward the positions usually found in diamagnetic compounds as the temperature decreases (Figure 5). Although the bis(ruthenium) complex [**3**]$(PF_6)_2$ was initially assigned as diamagnetic,[8b] the same experiment carried out with a solution of [**3**]$(PF_6)_2$ showed a shift of the Cp* methyl resonance from δ 1.93 to 1.52, while over the same temperature range, the broad ^{31}P signal continuously moved from δ 117.8 to 77.7. An experiment was carried out with a solution of [**8**]$(PF_6)_2$ and showed a shift of the Cp* methyl resonance from δ −0.86 to 1.45, while over the same temperature range, the Cp proton resonance shifts from δ 5.05 to 4.20. Similarly, in the case of the heterobimetallic compound [**7**]$(PF_6)_2$, δ_{Cp^*Fe} increases from −3.63 to −1.25 as the temperature decreases from 293 to 205 K, whereas the value for δ_{Cp^*Ru} decreases from 5.46 to 3.69.

Plots of the experimental chemical shifts against $1/T$ all display deviations from linearity. The solid lines drawn through the data points in Figure 5 correspond to the best fits of parameter J obtained for the compound [**7**]$(PF_6)_2$ (eq 2 above). For the three compounds [**3**]$(PF_6)_2$, [**7**]$(PF_6)_2$, and [**8**]$(PF_6)_2$, variations of the ^{1}H (Cp*Me/CpH) and ^{31}P resonances with $1/T$ could be fitted with the same set of parameters. The experimental J values increase from $J = -850$ cm^{-1} for [**3**]$(PF_6)_2$ through $J = -500$ cm^{-1} for [**7**]$(PF_6)_2$ to $J = -350$ cm^{-1} for [**8**]$(PF_6)_2$. The negative signs for the J values of the three compounds confirm that they all have singlet ground states as previously found for the bis(iron) dication in [**1**]$(PF_6)_2$. However, in the latter, the triplet state lies only 18 cm^{-1} above the singlet state. Substitution of one Fe atom by a Ru atom increases the gap to 500 cm^{-1}, and substitution of both Fe nuclei by two Ru nuclei increases it to 830 cm^{-1}. In other words, at 293 K the samples of [**3**]$(PF_6)_2$, [**7**]$(PF_6)_2$, [**8**]$(PF_6)_2$, and [**1**]$(PF_6)_2$ contain ca. 9, 20, 35, and 75%, respectively, of molecules in the triplet state. These results emphasize the aptitude of ruthenium to stabilize the singlet vs the triplet state. It is noteworthy that the calculated singlet/triplet energy differences are in reasonable agreement with the experimental results. The small discrepancies in experimental and calculated energies can be attributed to the use of model ligands and the variation in the dipole moments, which lead to differences in the solvation energy, and the intrinsic error of the theoretical method used (e.g., self-interaction, relativistic effects in Re-containing compounds, etc.).

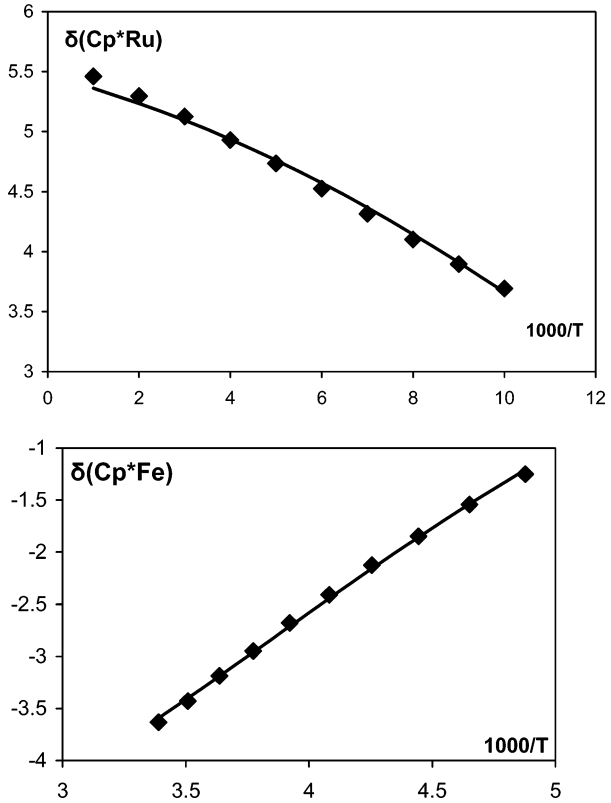

Figure 5. Plots of the observed (points) vs calculated (line) temperature dependence of δ_{Cp^*Ru} (top) and δ_{Cp^*Fe} in [**7**]$(PF_6)_2$ (bottom).

In the dication series, a very good linear correlation ($R = 0.99$, Figure 6) was found between the experimental singlet/triplet energy gaps and the spin densities on the metal atoms calculated by DFT methods. While this empirical relationship is not supported theoretically, it clearly shows that for the series of dications $[\mathbf{Fe}_2]^{2+}$, $[\mathbf{FeRe}]^{2+}$, $[\mathbf{FeRu}]^{2+}$, and $[\mathbf{Ru}_2]^{2+}$, the singlet/triplet energy differences increase linearly as the spin densities on the metal atoms decrease.

10. Electronic Absorption Spectroscopy. The UV−vis−NIR spectra of $[\mathbf{7}]^{n+}$ and $[\mathbf{8}]^{n+}$ ($n = 0-2$) were recorded in CH_2Cl_2 solution via spectro-electrochemical techniques (in which case the solution also contained

(30) La Mar, G. N.; Eaton, G. R.; Holm, R. H.; Walker, F. A. *J. Am. Chem. Soc.*, **1973**, *95*, 63.
(31) Weyland, T.; Costuas, K.; Mari, A.; Halet, J.-F.; Lapinte, C. *Organometallics* **1998**, *17*, 5569.
(32) Martin, R. L. In *New Pathways in Inorganic Chemistry*; Ebsworth, E. A. V., Maddock, A. G., Sharpe A. G., Eds.; Cambridge UP: London, 1968; pp 42−46.
(33) Roger, C.; Hamon, P.; Toupet, L.; Rabaâ, H.; Saillard, J.-Y.; Hamon, J.-R.; Lapinte, C. *Organometallics* **1991**, *10*, 1045.

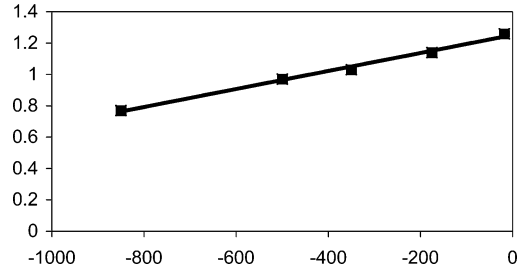

Figure 6. Plot of the *S*/*T* energy gap (cm^{-1}) vs computed spin densities on the metal atoms.

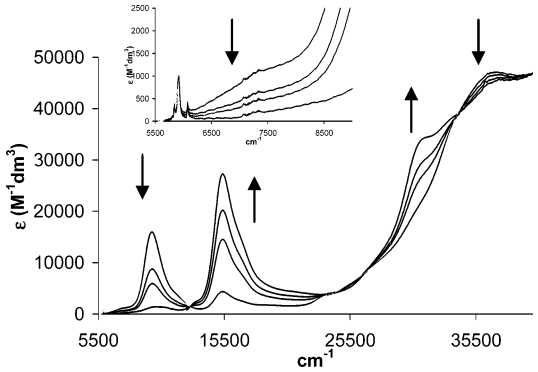

Figure 7. Spectroelectrochemical conversion of $[\mathbf{7}]^+$ to $[\mathbf{7}]^{2+}$. Arrows show the growth and decay of absorption bands during the oxidation event. The inset shows an expansion of the NIR region, illustrating the lowest energy band present in the monocation.

0.1 M $[NBu_4]BF_4$ as supporting electrolyte, Figure 7) and in pure solvent with the isolated materials. Not unexpectedly, the spectral profiles generated from **7** and **8** are similar with the substitution of the Ru(dppe)Cp* fragment in **7** for $Ru(PPh_3)_2Cp$ in **8**, having only a small effect on the energy and intensity of each band.

In addition to intense absorptions below 250 nm assignable to intraligand transitions involving the Cp and phosphine ligands, the electronic absorption spectra of the neutral species exhibit bands at 37 300 cm^{-1}/268 nm (**7**) or 37 700 cm^{-1}/265 nm (**8**), together with several other unresolved bands at lower energy, which tail into the visible region and are responsible for the colors of these complexes. Comparison with the related iron and ruthenium complexes Fe(C≡CPh)(dppe)Cp*,[20] $Fe(C{\equiv}CC{\equiv}CSiMe_3)$(dppe)Cp*, and $Ru(C{\equiv}CC{\equiv}CSiMe_3)$-(dppe)Cp*, which show low-energy absorptions at 348, 371, and 345 nm, respectively, enables the low-energy absorption bands to be tentatively assigned to a combination of $d_\pi(Fe) \rightarrow \pi^*(C{\equiv}C)$ and $d_\pi(Ru) \rightarrow \pi^*(C{\equiv}C)$ metal-to-ligand charge transfer (MLCT) transitions.

Upon oxidation, bands at lower energy (**8**: 37 000 cm^{-1}/270 nm; **7**: 37 300 cm^{-1}/268 nm) with discernible shoulders at 26 000 cm^{-1}/385 and 23 800 cm^{-1}/420 nm (**8**) or 23 800 cm^{-1}/420 nm (**7**) are observed. However, the most pronounced changes in the spectra arise in the vis−NIR region with the appearance of relatively intense bands, with a shoulder on the high-energy side, in the NIR region (**8**: 10 300 cm^{-1}/970 nm and 12 200 cm^{-1}/820 nm; **7**: 9900 cm^{-1}/1010 nm and 12 000 cm^{-1}/830 nm). The precise assignment of the NIR band is difficult without consideration of the electronic structure in some detail, as such low-energy bands usually result from transitions from lower-lying filled orbitals to the SOMO. At this point we simply note that similar low-energy absorption bands have also been observed in the related cations $[\mathbf{1}]^+$ (619 and 845 nm),[6a] [{Cp*(dppe)-Fe}CCCC{$Fe(CO)_2$Cp*}]PF_6 (829 nm),[6c] and $[\mathbf{3}]^+$ (714 and 816 nm)[8b] and in the heterobimetallic complex [{Cp*(dppe)Fe}CCCC{$Re(NO)(PPh_3)$Cp*}]PF_6 (868 nm).[9] In addition, very weak bands were also observed in the NIR region, with maxima at 7300 cm^{-1}/1370 nm ($[\mathbf{8}]^+$) and 7400 cm^{-1}/1350 nm^{-1} ($[\mathbf{7}]^+$). To limit the influence of ionic interactions on the spectra, the NIR spectra were re-recorded using the neat solutions of isolated PF_6 salts of the monocations $[\mathbf{8}]^+$ and $[\mathbf{7}]^+$ in pure CH_2Cl_2, which gave weak NIR absorptions at 7420 cm^{-1}/1347 nm and 7700 cm^{-1}/1298 nm, respectively. Further oxidation to the dication results in the collapse of these low-energy features, with the appearance of a higher energy transition near 15 500 cm^{-1} (Figure 7). Similar bands are also present in the electronic spectra of other 34-electron diyndiyl complexes and are assigned to LMCT transitions.

The determination of the nature and extent of the electronic coupling between redox sites in mixed-valence complexes has been a topic of fascination for decades and continues to pose many fundamental and challenging problems.[34] Theories initially developed by Hush have provided some of the primary theoretical tools necessary for unravelling some of these issues by linking the coupling term with the energy and band shape of the intervalence charge transfer band.[35] Physically, the IVCT band corresponds to the photoinduced electron transfer from a lower energy filled orbital of appropriate symmetry to the SOMO. Assuming a significant contribution from the Fe center to the first oxidation process, the lowest energy absorption band could be crudely approximated as an Ru(II) → Fe(III) charge transfer band. Typically, in nonsymmetric mixed-valence systems such as $[\mathbf{8}]^+$ and $[\mathbf{7}]^+$ the redox centers are weakly coupled and the Hush model should apply, although in the present case the computational and spectroscopic data support a more delocalized view of the bonding in these monocationic species, and such an interpretation must be regarded with a degree of caution.

If the Hush approximations are considered valid in the present case, the electronic coupling parameters V_{AB} can be calculated from eq 3, where $R_{MM'}$ is the electron transfer distance.

$$V_{AB} = 0.0205(\epsilon_{max}\bar{\nu}_{max}\Delta\bar{\nu}_{1/2})^{1/2}/R_{MM'} \qquad (3)$$

If one assumes the electron transfer distance to be approximately the same as the crystallographically determined through-bond Fe−Ru separation ($[\mathbf{8}]^+$ d_{Fe-Ru} = 7.63 Å; $[\mathbf{7}]^+$ d_{Fe-Ru} = 7.60 Å) and that $\Delta\bar{\nu}_{1/2}$ is approximately twice the bandwidth on the low-energy side ($\Delta\bar{\nu}_{1/2}$ ca. 1400 cm^{-1}), eq 3 yields electronic coupling terms of 230 cm^{-1} for $[\mathbf{8}]^+$ and 310 cm^{-1} for $[\mathbf{7}]^+$. Both values are larger than the value obtained for $[\mathbf{6}]PF_6$ (V_{AB} = 152 cm^{-1}),[9] and they approach the higher values reported in the literature for nonsymmetrical mixed-valence complexes.[26] In addition, it is important to keep

(34) (a) *Mixed Valency Systems—Applications in Chemistry, Physics and Biology*; Prassides, K., Ed.; Kluwer Academic Publishers: Dordrecht, 1991. (b) Cruetz, C. *Prog. Inorg. Chem.* **1983**, *30*, 1. (c) Brunschwig, B. S.; Cruetz, C.; Sutin, N. *Chem. Soc. Rev.* **2002**, *31*, 168.
(35) Hush, N. S. *Coord. Chem. Rev.* **1985**, *64*, 135.

in mind that the Hush model provides underestimated values when the electronic couplings become significant.[36]

Conclusions

The new heterobimetallic complexes {Cp*(dppe)Fe}C≡CC≡C{Ru(dppe)Cp*} (**7**) and {Cp*(dppe)Fe}C≡CC≡C{Ru(PPh$_3$)$_2$Cp} (**8**) have been obtained in good yields by coupling Ru(C≡CC≡CH)(dppe)Cp* or Ru(C≡CC≡CH)(PPh$_3$)$_2$Cp with FeCl(dppe)Cp* in a mixed thf/NEt$_3$ solvent, in the presence of dbu and Na[BPh$_4$]. Stepwise chemical oxidation with [FeCp$_2$]PF$_6$ gave the mono- and dications, [**7**](PF$_6$)$_n$ and [**8**](PF$_6$)$_n$ (n = 1, 2), with the available X-ray structural data consistent with the gradual evolution of the polycarbon moiety from a diyndiyl structure to a more cumulenic system.

Computational work indicates these heterometallic systems are well described in terms of a delocalized electronic structure, with a significant contribution from the iron center to the highest lying orbitals. These conclusions are in complete agreement with ^{57}Fe Mössbauer, ESR, IR, UV−vis, and NIR spectroscopic results. Detailed analysis of the NIR region is complicated by the overlapping of the lowest energy band with several other transitions, but in light of the electronic structure, this transition can be approximated as arising from a photoinduced electron transfer from iron to ruthenium.

The dioxidized complex [**8**](PF$_6$)$_2$ most likely has a structure intermediate between the diyndiyl and cumulenic forms with a singlet ground state. No signal is found in the ESR spectra even at liquid helium temperature. Although the ^{13}C resonances of the carbon chain atoms could not be observed, the IR spectrum shows a decrease in the ν(CC) frequency, consistent with the evolution of a cumulenic character in the C$_4$ moiety upon oxidation. Taken together, the data indicate the dominant role of ruthenium over iron in dictating the underlying electronic structures of C$_4$-bridged bimetallic complexes. For the first time this work clearly shows the critical role of the nature of the metal centers and allows an estimation of the relative contributions of the metal and ancillary ligands to the properties of the [{M}−CC−CC−{M}]$^{n+}$ assemblies.

Experimental Section

General Data. All reactions were carried out under dry, high-purity argon using standard Schlenk techniques. Common solvents were dried, distilled under argon, and degassed before use.

Instruments. Infrared spectra were obtained on a Bruker IFS28 FT-IR spectrometer. Spectra in CH$_2$Cl$_2$ were obtained using a 0.5 mm path length solution cell with NaCl windows. Nujol mull spectra were obtained from samples mounted between NaCl disks. NMR spectra were recorded on a Varian 2000 instrument (^{1}H at 300.13 MHz, ^{13}C at 75.47 MHz, ^{31}P at 121.503 MHz). Unless otherwise stated, samples were dissolved in CDCl$_3$ contained in 5 mm sample tubes. Chemical shifts are given in ppm relative to internal tetramethylsilane for ^{1}H and ^{13}C NMR spectra and external H$_3$PO$_4$ for ^{31}P NMR spectra. UV−vis spectra were recorded on a Varian Cary 5 UV−vis/NIR spectrometer. Electrospray mass spectra (ES-MS) were obtained from samples dissolved in MeOH unless otherwise indicated. Solutions were injected into a VG Platform II spectrometer via a 10 mL injection loop. Nitrogen was used as the drying and nebulizing gas. Chemical aids to ionization were used.[39] Electrochemical samples (1 mM) were dissolved in CH$_2$Cl$_2$ with 0.5 M [NBu$_4$]BF$_4$ as the supporting electrolyte for the spectro-electrochemical experiments. Cyclic voltammograms were recorded using a PAR model 263 apparatus, with a saturated calomel electrode and with ferrocene as internal calibrant ($FeCp_2/[FeCp_2]^+$ = 0.46 V). A 1 mm path length cell was used with a Pt-mesh working electrode, Pt wire counter electrode, and pseudoreference electrodes. The OTTLE cell has been described elsewhere.[40] X-Band ESR spectra were recorded on a Bruker ESP-300E spectrometer. Mössbauer spectra were recorded with a 2.5 × 10^{-2} Ci (9.25 × 10^8 Bq) ^{57}Co source using a triangular sweep mode.[41] Elemental analyses were performed by the Centre pour Microanalyses du CNRS, Vernaison, France, and CMAS, Belmont, Vic., Australia.

Reagents. Na[BPh$_4$] (Aldrich) and [NBu$_4$]F (Aldrich) were used as received. The compounds FeCl(dppe)Cp*,[33] RuCl(PPh$_3$)$_2$Cp,[42] RuCl(dppe)Cp*,[8b] Ru(C≡C≡CH)(PP)Cp′ [PP = (PPh$_3$)$_2$, Cp′ = Cp; PP = dppe, Cp′ = Cp*],[10] and [FeCp$_2$]PF$_6$ [43] were prepared using the cited methods.

{Cp*(dppe)Fe}C≡CC≡C{Ru(dppe)Cp*} (7). A Schlenk flask containing Ru(C≡CC≡CH)(dppe)Cp* (250 mg, 0.365 mmol), FeCl(dppe)Cp* (228 mg, 0.365 mmol), and Na[BPh$_4$] (162 mg, 4.75 mmol) was dried under vacuum. A mixture of NEt$_3$ (30 mL) and dbu (109 mg, 0.72 mmol) was added via cannula, and the suspension was stirred at rt for 24 h. The resulting light brown suspension was evaporated to dryness and the resulting solid extracted into Et$_2$O (2 × 20 mL) and filtered via cannula into a second Schlenk flask. The solvent was removed and the solid was washed with methanol (2 × 10 mL) before being dried under vacuum to give {Cp*(dppe)Fe}C≡CC≡C{Ru(dppe)Cp*} (**7**) as a brick-red powder (335 mg, 73%). Anal. Found: C, 71.64; H, 6.23. Calcd (C$_{62}$H$_{78}$FeP$_4$Ru): C, 71.68; H, 6.18. M = 1272. IR (Nujol): ν(CC) 1966w cm^{-1}. ^{1}H NMR: δ 1.59 (s, 15H, Fe-Cp*), 1.82 (s, 15H, Ru-Cp*), 2.06, 2.85 (2m, 2 × 4H, CH$_2$CH$_2$), 7.14−8.26 (m, 40H, Ph). ^{13}C NMR: δ 10.50 (s, Ru-C$_5$*Me$_5$*), 10.56 (s, Fe-C$_5$*Me$_5$*), 30.05 (m, Ru-dppe), 31.52 (m, Fe-dppe), 87.43 (s, Fe-*C$_5$*Me$_5$), 92.53 (s, Ru-*C$_5$*Me$_5$), 93.57 (s, Ru-C≡*C*), 99.92 (s, Ru-*C*≡), 100.75 (br, ≡C-Fe), 109.70 (s, *C*≡C-Fe), 124.80−140.68 (m, Ph). ^{31}P NMR: δ 101.90 (br, Fe-dppe), 82.55 (br, Ru-dppe). FAB-MS (*m/z*): 1272, M$^+$; 1195, [M − Ph]$^+$; 874, [M − dppe]$^+$; 635, [Ru(dppe)Cp*]$^+$; 589, [Fe(dppe)Cp*]$^+$.

[{Cp*(dppe)Fe}C≡CC≡C{Ru(dppe)Cp*}]PF$_6$ ([7]PF$_6$). To a solution of **7** (500 mg, 0.39 mmol) in CH$_2$Cl$_2$ (20 mL) was added [FeCp*$_2$]PF$_6$ (123 mg, 0.37 mmol). The color quickly changed to brown, and the solution was stirred at rt for 2 h. Toluene (20 mL) was added, and the solution was filtered via cannula into another Schlenk tube. The solution was concentrated to 20 mL when crystallization began. The black crystal-

(36) The critical assumptions made in this analysis are open to debate. The difficulties associated with determining the electron transfer distance have been well documented, especially in systems within which the orbitals involved in the electron transfer process are delocalized over several atomic sites.[37] Curtis and co-workers have described an electrochemical approach for the assessment of the coupling parameter,[38] but any meaningful attempt to use this methodology in the present case of heterometallic diyndiyl complexes would require oxidation potentials to be collected from a much greater range of complexes than represented here.

(37) (a) Mines, G. A.; Roberts, J. A.; Hupp, J. T. *Inorg. Chem.* **1992**, *31*, 125. (b) Vance, F. W.; Slone, R. V.; Stern, C. L.; Hupp, J. T. *Chem. Phys.* **2000**, *253*, 313.

(38) Salaymeh, F.; Berhane, S.; Yusof, R.; de la Rosa, R.; Fung, E. Y.; Matamoros, R.; Lau, K. W.; Zheng, Q.; Kober, E. M.; Curtis, J. C. *Inorg. Chem.* **1993**, *32*, 3895.

(39) Henderson, W.; McIndoe, J. S.; Nicholson, B. K.; Dyson, P. J. *J. Chem. Soc., Dalton Trans.* **1998**, 519.

(40) Duff, C. M.; Heath, G. A. *Inorg. Chem.* **1991**, *30*, 2528.

(41) Greenwood, N. N. *Mössbauer Spectroscopy*; Chapman & Hall: London, 1971.

(42) Bruce, M. I.; Hameister, C.; Swincer, A. G.; Wallis, R. C. *Inorg. Synth.* **1990**, *28*, 270.

Table 12. Crystal Data and Refinement Details

	7·CH_2Cl_2	**7**·C_6H_6	[**7**]PF_6	[**7**]$(PF_6)_2$	**8**	[**8**]PF_6
formula	$C_{76}H_{78}FeP_4Ru$·CH_2Cl_2	$C_{76}H_{78}FeP_4Ru$·C_6H_6	$C_{76}H_{78}F_6FeP_5Ru$	$C_{76}H_{78}F_{12}FeP_6Ru$·$2CH_2Cl_2$	$C_{81}H_{74}FeP_4Ru$·$0.5CH_2Cl_2$	$C_{81}H_{74}F_6FeP_5Ru$
MW	1357.21	1350.39	1417.14	1747.98	1370.76	1473.26
cryst syst	triclinic	triclinic	monoclinic	triclinic	triclinic	triclinic
space group	$P\bar{1}$	$P\bar{1}$	$P2_1/n$	$P\bar{1}$	$P\bar{1}$	$P\bar{1}$
a, Å	10.955(2)	10.9250(7)	8.5154(5)	12.9851(2)	12.246(2)	13.241(2)
b, Å	17.776(3)	17.892(1)	20.070(1)	15.3597(2)	15.975(3)	14.279(2)
c, Å	17.809(3)	17.678(1)	19.316(1)	21.9668(3)	17.889(3)	20.629(3)
α, deg	88.888(4)	89.292(2)		73.8673(7)	80.484(3)	102.330(2)
β, deg	88.098(4)	88.455(2)	90.503(2)	89.2884(6)	86.577(3)	91.366(2)
γ, deg	85.405(5)	85.264(2)		66.3856(5)	76.503(3)	111.702(2)
V, Å^3	3455	3442	3301	3832	3355	3518
Z	2	2	2	2	2	2
D_c, g cm^{-3}	1.30_5	1.30_3	1.42_6	1.51_5	1.35_7	1.39_1
μ, cm^{-1}	0.64	0.57	0.63	0.726	0.62	0.60
cryst size, mm	0.25 × 0.18 × 0.08	0.39 × 0.28 × 0.22	0.2 × 0.15 × 0.08	0.33 × 0.26 × 0.24	0.15 × 0.11 × 0.04	0.58 × 0.45 × 0.15
$T_{min/max}$	0.80	0.80	0.81	none	0.69	0.75
$2\theta_{max}$, deg	58	58	60	55	50	50
N_{tot}	73 052	70 172	60 244	17 415	33 967	35 393
N (R_{int})	18 355 (0.067)	18 222 (0.062)	9470(0.062)	17 415 (0.047)	11 756 (0.067)	12 082 (0.045)
N_o	10 568	15 475	7266	14 122	7387	9469
R	0.051	0.057	0.038	0.058	0.059	0.054
R_w	0.054	0.098	0.046	0.074	0.079	0.081

line solid was filtered on a glass frit and washed with toluene (2 × 10 mL) followed by pentane (2 × 10 mL) to give [{Cp*(dppe)Fe}C≡CC≡C{Ru(dppe)Cp*}]PF_6 ([**7**]PF_6) (475 mg, 91%). Anal. Found: C, 64.43; H, 5.41. Calcd ($C_{62}H_{78}F_6FeP_5Ru$): C, 64.41; H, 5.55. M (cation) = 1272. IR (Nujol): ν(CC) 1986m (br), 1877w; ν(PF) 839s cm^{-1}.

[{Cp*(dppe)Fe}C≡CC≡C{Ru(dppe)Cp*}](PF$_6$)$_2$ ([7](PF$_6$)$_2$). To a solution of [**7**]PF_6 (400 mg, 0.28 mmol) in CH_2Cl_2 (20 mL) was added [$FeCp^*_2$]PF_6 (91.2 mg, 0.27 mmol). The brown solution quickly turned bright blue, and the solution was allowed to stir at rt for 2 h. Toluene (20 mL) was added, and the solution was filtered via cannula into another Schlenk flask before being concentrated under vacuum to 20 mL to initiate crystallization. The dark blue crystalline solid was filtered on a glass frit and washed with toluene (2 × 10 mL) and pentane (2 × 10 mL) to give [{Cp*(dppe)Fe}C≡CC≡C{Ru(dppe)Cp*}]$(PF_6)_2$ ([**7**]$(PF_6)_2$) (431 mg, 98%). Anal. Found: C, 58.25; H, 4.89. Calcd ($C_{76}H_{78}F_{12}FeP_6Ru$): C, 58.43; H, 5.03. M (dication) = 1272. IR (Nujol): ν(CC) 1870w, 1783s; ν(PF) 838s cm^{-1}. ^{1}H NMR (d_6-acetone): δ −3.83 (s, 15H, Fe-Cp*), −0.22 [s(br), 2H, CH_2], 2.88 (s, ortho-Ph), 3.04, 3.82, 4.26 [3 × s(br), 3 × 2H, 3 × CH_2], 5.46 (s, 15H, Ru-Cp*), 6.80−9.40 (m, Ph). ^{31}P NMR (d_6-acetone): δ −143.6 (septet, PF_6), 51.24 (br, Ru-dppe), 291.83 (br, Fe-dppe).

{Cp*(dppe)Fe}C≡CC≡C{Ru(PPh$_3$)$_2$Cp} (8). Ru(C≡CC≡CH)$(PPh_3)_2$Cp (422 mg, 0.57 mmol), FeCl(dppe)Cp* (338 mg, 0.57 mmol), and Na[BPh_4] (195 mg, 0.57 mmol) were dried in a Schlenk flask under vacuum. A mixture of thf/NEt_3 (1/1, 60 mL) and dbu (173 mg, 1.14 mmol) was added via cannula, and the solution was stirred at rt for 48 h. After evaporation of the solvent, an Et_2O extract (2 × 5 mL) of the residue was filtered via cannula into a second Schlenk flask. The combined filtrates were evaporated in a vacuum to give a dark brown solid, which was washed with MeOH (2 × 10 mL) and pentanes (2 × 10 mL) and dried under vacuum to give burnt orange {Cp*(dppe)Fe}C≡CC≡C{Ru$(PPh_3)_2$Cp} (**8**) (568 mg, 77%). Anal. Found: C, 72.69; H, 5.89. Calcd ($C_{81}H_{74}FeP_4Ru$): C, 73.24; H, 5.62. M = 1328. IR (Nujol): ν(CC) 1965w cm^{-1}. ^{1}H NMR: δ 1.66 (br, 15H, Fe-Cp*), 1.98, 3.01 (2 × m, 2 × 2H, 2 × CH_2), 4.40 (s, 5H, Ru-Cp), 7.15−8.41 (m, 50H, Ph). ^{13}C NMR: δ 10.45 (s, Fe-C_5Me_5), 30.02 (s, CH_2), 81.98 (s, Fe-C_5Me_5), 85.68 (s, Ru-C_5H_5), 127.41−142.16 (m, Ph). ^{31}P NMR: δ 52.43 (s, PPh_3), 101.77 (s, dppe).

[{Cp*(dppe)Fe}C≡CC≡C{Ru(PPh$_3$)$_2$Cp}]PF$_6$ ([8]PF$_6$). A Schlenk flask was charged with **8** (500 mg, 0.376 mmol), [$FeCp_2$]PF_6 (118 mg, 0.356 mmol), and CH_2Cl_2 (25 mL). The resulting brown solution was stirred at rt for 1.5 h and then concentrated to ca. 5 mL, and pentane (100 mL) was added. The resulting dark green-brown precipitate was collected and washed with toluene (2 × 5 mL), Et_2O (2 × 5 mL), and pentane (2 × 10 mL) and dried under vacuum to give [{Cp*(dppe)Fe}C≡CC≡C{Ru$(PPh_3)_2$Cp}]PF_6 ([**8**]PF_6) (505 mg, 96%). Anal. Found: C, 66.13; H, 5.42. Calcd ($C_{81}H_{74}F_6FeP_5Ru$): C, 66.04; H, 5.06. M (cation) = 1328. IR (Nujol): ν(CC) 1956 (br), 1883 (sh); ν(PF) 840s cm^{-1}.

[{Cp*(dppe)Fe}C≡CC≡C{Ru(PPh$_3$)$_2$Cp}](PF$_6$)$_2$ ([8](PF$_6$)$_2$). A Schlenk flask was charged with [**8**]PF_6 (300 mg, 0.20 mmol), [$FeCp_2$]PF_6 (67.4 mg, 0.20 mmol), and CH_2Cl_2 (20 mL). The solution turned deep blue immediately. Stirring was continued at rt for a further 1 h, and the solution was concentrated to ca. 5 mL before pentane (100 mL) was added. The resulting blue precipitate was collected and washed with Et_2O (2 × 5 mL) and pentane (2 × 10 mL) and dried under vacuum to give deep blue [{Cp*(dppe)Fe}C≡CC≡C{Ru$(PPh_3)_2$Cp}]$(PF_6)_2$ ([**8**]$(PF_6)_2$) (300 mg, 93%). Anal. Found: C, 55.75; H, 4.21. Calcd ($C_{81}H_{74}F_{12}FeP_6Ru.2CH_2Cl_2$): C, 55.75; H, 4.40. M (dication) = 1328. IR (Nujol): ν(CC) 1890 (br), 1781m; ν(PF) 840s cm^{-1}. ^{1}H NMR (CD_2Cl_2): δ −0.86 (s, 15H, Fe-Cp*), 1.61, 3.21 (2 × m, 2 × 2H, 2 × CH_2), 5.05 (s, 5H, Ru-Cp), 6.65−7.98 (m, 50H, Ph). ^{13}C NMR (CD_2Cl_2): δ 1.00 (s, C_5Me_5), 10.26 (m, CH_2), 88.26 (s, C_5Me_5), 90.95 (s, Ru-Cp), 128.11−136.73 (m, Ph). ^{31}P NMR (CD_2Cl_2): δ −143.47 (septet, PF_6), 42.91 (s, PPh_3), 86.24 (s, dppe).

Structure Determinations. Full spheres of diffraction data to the indicated limits were measured at ca. 153 K using either Bruker AXS CCD or Nonius Kappa (for [**7**]$(PF_6)_2$) area-detector instruments. N_{tot} reflections were merged to N unique (R_{int} quoted) after "empirical"/multiscan absorption correction (proprietary software), N_o with $F > 4\sigma(F)$ being used in the full matrix least squares refinement. All data were measured using monochromatic Mo Kα radiation, λ = 0.71073 Å. Anisotropic displacement parameter forms were refined for the non-hydrogen atoms, (x, y, z, U_{iso})$_H$ being constrained at estimated values. Conventional residuals R, R_w on $|F|$ are given [weights: $(\sigma^2(F) + 0.0004F^2)^{-1}$]. Neutral atom complex scattering factors were used; computation used the XTAL 3.7 program system.[44] Typical results are given in Figure 2 (which show non-hydrogen atoms with 50% probability amplitude

(43) Connelly, N. G.; Geiger, W. E. *Chem. Rev.* **1996**, *96*, 877.
(44) Hall, S. R.; du Boulay, D. J.; Olthof-Hazekamp, R., Eds. *The XTAL 3.7 System*; University of Western Australia, 2000.

displacement ellipsoids and hydrogen atoms with arbitrary radii of 0.1 Å) and Tables 4 and 12. In all derivatives of **7**, Ru and Fe were modeled as disordered over the pair of M sites, occupancies 0.5 each.

Variata. 7. Refinement of the benzene solvate was unproblematical, albeit with high displacement parameters (unresolved disorder?) for the solvent molecule. In the isomorphous CH_2Cl_2 solvate, the solvent was modeled as disordered over a pair of sites of equal occupancy.

[7]PF_6. (x, y, z, U_{iso})$_H$ were refined throughout.

[7]$(PF_6)_2$. Data reduction,[45] structure solution,[46] and refinement[47] used the cited methods.

8. Difference map residues were modeled as a pair of CH_2Cl_2 fragments, occupancies set at 0.25 after trial refinement.

Theoretical Calculations. Density functional theory (DFT) calculations were carried out on model compounds derived from the experimental structure data using the Amsterdam Density Functional (ADF) program,[48] developed by Baerends and co-workers.[49] Electron correlation was treated within the local density approximation (LDA) in the Vosko−Wilk−Nusair parametrization.[50] The nonlocal corrections of Becke and Perdew were added to the exchange and correlation energies, respectively.[51,52] The numerical integration procedure applied for the calculations was developed by te Velde et al.[49e] The atom electronic configurations were described by a triple-ζ Slater-type orbital (STO) basis set for H 1s, C 2s and 2p, N 2s and 2p, O 2s and 2p, and P 3s and 3p augmented with a 3d single-ζ polarization for C, N, O, and P atoms and with a 2p single-ζ polarization for H atoms. A triple-ζ STO basis set was used for Fe 3d and 4s and Ru 4d and 5s augmented with a single-ζ 4p polarization function for Fe and a single-ζ 5p polarization function for Ru. A double-ζ STO basis set was used for Re 5s and a triple-ζ STO basis set was used for Re 4f, 5p, 5d augmented with a single-ζ 6p polarization function. A frozen-core approximation was used to treat the core shells up to 1s for C, N, and O, 2p for P, 3p for Fe, 4p for Ru, and 4d for Re.[48] Full geometry optimizations were carried out using the analytical gradient method implemented by Verluis and Ziegler.[53] Spin-unrestricted calculations were performed for all the open-shell systems. Representation of the molecular orbitals was done using MOLEKEL4.1.[54]

Energy decomposition of the M−C bond in the C_4-containing bimetallic complexes was done according to the *transition state* method of Ziegler and Rauk.[16b,46d] In this method, the interaction energy can be split up into three different physically meaningful terms: $\Delta E = \Delta E_{el} + \Delta E_{orb} + \Delta E_{Pauli}$. ΔE_{el} is the classical electrostatic interaction between the charge distributions of the interacting fragments in their unrelaxed geometry and is generally attractive (>0). ΔE_{Pauli} roughly corresponds to the repulsive energy issued from the interaction between the occupied orbitals of the fragments. ΔE_{orb} mainly accounts for the interaction between occupied and vacant orbitals and therefore can be considered as an estimate of the covalent contributions to the bonding.

Acknowledgment. We thank the Australian Research Council (M.I.B., A.H.W.) and the EPSRC (P.J.L.) for support of this work and Johnson Matthey plc, Reading, UK, for a generous loan of $RuCl_3 \cdot nH_2O$. K.C. and J.-F.H. thank the Pôle de Calcul Intentif de l'Ouest (PCIO) of the University of Rennes and the Institut de Développement et de Ressources en Informatique Scientifique (IDRIS-CNRS) for computing facilities. These studies were facilitated by travel grants (ARC, Australia, the Royal Society, UK, and CNRS, France).

Supporting Information Available: Cif files for **7** (as benzene and dichloromethane solvates), [**7**]PF_6, [**7**]$(PF_6)_2$, **8**, [**8**]PF_6, and [**8**]$(PF_6)_{1.5}$, together with a description and interpretation of the latter structure. This material is available free of charge via the Internet at http://pubs.acs.org.

OM050293A

(45) Otwinowski, Z.; Minor, W. Processing of X-ray Diffraction Data Collected in Oscillation Mode. In *Methods in Enzymology*, Vol. 276, *Macromolecular Crystallography, Part A*; Carter, C. W.; Sweet, R. M., Ed.; Academic Press: London, 1997; pp 307−326.

(46) Altomare, A.; Burla, M. C.; Camalli, M.; Cascarano, G.; Giacovazzo, G.; Guagliardi, A.; Moliterni, A. G. G.; Polidori, G.; Spagna, R. Sir97: a new tool for crystal structure determination and refinement. *J. Appl. Crystallogr.* **1998**, *31*, 74.

(47) Sheldrick, G. M. *SHELX97, Program for the Refinement of Crystal Structures*; University of Gottingen, Germany, 1997.

(48) *ADF2002.01, Theoretical Chemistry*; Vrije Universiteit: Amsterdam, The Netherlands, SCM.

(49) (a) Baerends, E. J.; Ellis, D. E.; Ros, P. *Chem. Phys.* **1973**, *2*, 41. (b) te Velde, G.; Baerends, E. J. *J. Comput. Phys.* **1992**, *99*, 84. (c) Fonseca Guerra, C.; Snijders, J. G.; te Velde, G.; Baerends, E. J. *Theor. Chim. Acc.* **1998**, *99*, 391. (d) Bickelhaupt, F. M.; Baerends, E. J. *Rev. Comput. Chem.* **2000**, *15*, 1. (e) te Velde, G.; Bickelhaupt, F. M.; Fonseca Guerra, C.; van Gisbergen, S. J. A.; Baerends, E. J.; Snijders, J. G.; Ziegler, T. *J. Comput. Chem.* **2001**, *22*, 931.

(50) Vosko, S. D.; Wilk, L.; Nusair, M. *Can. J. Chem.* **1990**, *58*, 1200.

(51) Becke, A. D. *J. Chem. Phys.* **1986**, *84*, 4524. (b) Becke, A. D. *Phys. Rev. A* **1988**, *38*, 3098.

(52) Perdew, J. P. *Phys. Rev. B* **1986**, *33*, 8822. (b) Perdew, J. P. *Phys. Rev. B* **1986**, *34*, 7406.

(53) Verluis, L.; Ziegler, T. *J. Chem. Phys.* **1988**, *88*, 322.

(54) Flükiger, P.; Lüthi, H. P.; Portmann, S.; Weber, J. *MOLEKEL4.1*; Swiss Center for Scientific Computing (CSCS): Switzerland, 2000−2001.